OPTICAL TWEEZERS: Characterization and Systems Approach to High Bandwidth Force Estimation

A DISSERTATION
SUBMITTED TO THE FACULTY OF THE GRADUATE SCHOOL
OF THE UNIVERSITY OF MINNESOTA
BY

Hullas Sehgal

IN PARTIAL FULFILLMENT OF THE REQUIREMENTS
FOR THE DEGREE OF
Doctor Of Philosophy

Advisor: Dr. Murti V. Salapaka

April, 2010

Acknowledgements

Life as a PhD student is a mixed bag. On one hand, you get to work on something new, something fundamental and make an original contribution. And not to forget, it offers the chance to be a student in a protected zone that a university offers along with a lot of young people around makes for a comfortable environment. On the flip side, the commitment that PhD requires in terms of effort and number of years can be a dampener of spirits for many. The answer to this conundrum listing the merits and demerits of doing a PhD differs widely depending on who you ask. However, what remains indisputable is this long arduous journey can become a smooth enjoyable ride in the company of friends, co-operative colleagues, support of family and most importantly a helpful advisor.

I would like to take this opportunity to express my deepest gratitude to all those, who have made my stay as a graduate student easier. During the initial period of my PhD, Anil Gannepalli guided me through the process of creating an optical trap. He was at the end of his PhD back then and had developed a methodical approach to getting things done. But working with a new recruit in the NDSL lab like myself, he remained patient and empathetic to my pace of understanding. Then there was Abu Sebastian - who graduated about a year after I became part of the NDSL group. I did not specifically work with Abu on any project, however his work ethics were exemplary and an inspiration.

Deepak Sahoo, Tathagata De and Vikas Yadav were my colleagues and great friends in NDSL lab. I did a few courses with them and sometimes used their notes from previous years. These are the guys I would hang around with, have lunch with and go for movies till their graduation. Vikas was also my batchmate during undergraduate years and my room-mate during my time at Iowa State University. I have known Pranav

Agarwal since 1996 and he has been my room-mate for the last 6 years. He too is part of NDSL lab, is a very close friend and a confidant. I have almost invariably turned to him in the hour of need - be it a problem related to work or otherwise, and fortunately for me, I was never disappointed barring this one time when I confided in him and he let others know about it or when he borrowed my full sized suitcase to travel to India and never return it or on those numerous occasions when he skipped his cooking turn for no valid reason and the list goes on and on and on.

In terms of pure dedication to work, I have been most influenced by colleague and also my present room-mate - Tanuj Aggarwal. Tanuj and I both work with the optical tweezers setup. I had introduced him to optical tweezers after he joined our Lab, but in no time he became an expert on the subject. I have collaborated with him on many projects, authored papers with him and he has been extremely helpful in getting things moving. He can work like a robot for very long hours without a break and has a knack for instrumentation. He is a gem of a person and its been my honor to have him as a colleague and pleasure to be his friend.

I am grateful to Vipul Katyal, Shourya Otta and Bipin Singh for being around when it mattered. Vipul, a batchmate from undergraduate days was my room-mate at Iowa State University. A strict disciplinarian by nature, his presence helped maintaining a schedule. Shourya - again a batchmate from undergraduate days and a would be colleague at GE Research - I want to tell you - Thank you. With Bipin, I have some very fond memories of graduate school.

Donatello Materassi - my partner in long distance running and sometimes referred to as my *evil twin*. His crooked sense of humor often brought an element of lightness to an otherwise dull routine. During this long course as a PhD student, I have gotten to know many different people. Some of them I must mention here are Govind Saraswat, Rajat Mittal and Pushkar Modi. These are my friends, I can take for granted without them getting offended. I will remember the time spent with Manoj Paul and Subhrajit Roychowdhury for all the good reasons.

Durga Kocherlakota is one person I really admire for her simplicity and serene disposition. She is a friend, my advisors wife and an amazing cook. She has hosted lunch and dinner for our entire group countless times and I am going to miss her parties, when I am gone from here. Many a times, we look back at those halcyon days when we

were young and long for them. Sidharth Salapaka and Pranav Salapaka are two very naughty kids, who allow me to stay connected with this romantic notion of staying a kid forever and often brings a tranquilizing smile with their innocent antics.

Family typically plays a big role in who a person becomes. I feel blessed to have very understanding parents and a very loving sister. They have been a source of constant support and encouragement, throughout my life. They are my emotional lifeline who have always provided for me. I could not have gotten this far without them and I want to take this opportunity to tell them - I love you.

Dr Murti Salapaka is my advisor, my mentor, my guru. I consider myself very fortunate to have worked under his supervision. I have been extremely impressed and inspired by his motivation, his mental acumen, his dedication to his cause and above all his uprighteousness. Unlike many graduate students who have only a professional relationship with their advisors, I have gotten to know Dr. Murti on a personal level too. I feel honored to be associated with him and shall forever remain indebted for all he has done for me. Sir, I have the highest respect for you and will strive to make you proud of me.

Dedication

To my parents and sister, who have been a source of continuous support and encouragement during my graduate school.

ABSTRACT

In recent times, the hard boundaries between classical fields of sciences have almost disappeared. There is a cross-pollination of ideas between sciences, engineering and mathematics. This work investigates a modern tool of micro-manipulation of microscopic particles that is used primarily by bio-physicists and bio-chemists for single cell, single molecule studies. This tool called the Optical Tweezers can trap microscopic dielectric particles using radiation pressure of light. Optical tweezers is increasingly being used in bio-assays as it provides a means to observe bio-molecules non invasively and offers a spatial resolution in nanometers and force resolution in femto-Newtons at millisecond timescales.

In this work, physics governing the operating principle behind optical tweezers is presented, followed by a step by step procedure to build an optical tweezers system having measurement and actuation capability along with a controller logic for feedback implementation. The working of optical tweezers system is presented using a spring mass damper model and the traditional methods of optical tweezers characterization are discussed. A comprehensive view of Optical tweezers is then presented from a system theoretic perspective, underlying the limitations of traditional methods of tweezers characterization that are based on the first principle. The role of feedback in Optical tweezers is presented along with the fundamental limitations that the plant model imposes on optical tweezers performance to be used as a force sensor for fast dynamics input force. The purpose of optical tweezers as a pico-newton force probe is emphasized and a classical controls based method to improve the bandwidth of force estimation using an ad-hoc approach of system inversion is presented. The efficacy of system inversion based method in improving the force probe capability of feedback enhanced optical tweezers is validated by experimental results. It is shown experimentally that the system inversion method results in an order of magnitude improvement in the bandwidth of external force estimation. Finally, a robust control strategy is presented, where the problem of estimation of high bandwidth force is casted as an H-infinity optimization problem along with other performance objectives. This strategy is then compared with the traditional method using PI-controllers and experimental results presented. The

robust control strategy is found to further improve the ability of optical tweezers as a force sensor for fast changing force profile by approximately three times over the system inversion approach.

Contents

List of Figures

Chapter 1

INTRODUCTION

The advent of micro and nano-manipulation tools in the past two decades has ushered in an era of experimental studies of the building blocks of life. This period has witnessed a shift in focus from aggregate to single cell and single molecule studies. This change can be attributed to the invention of micro-manipulation tools that include Scanning tunneling Microscope (STM) [1], Atomic Force Microscope (AFM) [2], Optical Tweezers [3] and Single Molecule Fluorescence Microscope [4]. These tools have equipped scientists to do exciting studies involving interaction between single biological molecules, like motor protein interactions with actin filament or microtubule [5, 6], or the process of DNA transcription involving a DNA strand and its corresponding protein [7]. They offer high temporal and spatial resolution along with being non invasive to various kinds of specimens, thereby enabling the study of force dynamics of single cell interactions.

The focus of this research work is Optical tweezers. Optical tweezers use the radiation pressure of a highly convergent laser beam to form a stable 3-D trap for micron sized dielectric particles. In 1970 Ashkin discovered that the forces caused by radiation pressure of lasers can be used to change the dynamics of micron sized particles that are neutral and transparent. Such forces were experimentally shown to lead to a stable 3-D trap for micron sized particles. In [8] Ashkin demonstrated the use of lasers to levitate particles using focused laser beams. During these experiments Ashkin discovered that the particles not only get accelerated in the direction of the laser beam, due to scattering forces, but that the particles moved in a direction where the intensity of the laser beam is a maximum that was attributed to gradient forces. A schematic showing

a qualitative picture of the force vectors due to scattering forces and gradient forces due to two rays A and B emerging from a light beam having a Gaussian intensity profile is shown in Figure 1.1(a). In this figure, the scattering forces due to the two rays A and B are in the direction of the respective emergent refracted rays. The gradient force due to rays A and B (shown in the figure) are $F^{A}_{gradient}$ and $F^{B}_{gradient}$ respectively and is in the direction of light rays A and B. The resultant gradient force vector, F_{net}, (shown in Figure 1.1(a)) is towards the ray A as it has a higher intensity than ray B due to a Gaussian intensity profile. In [3] it was shown that the gradient force for dielectric particles can be large enough to dominate the axial stability and counteract the scattering forces. In the related experiments only one beam, that is focused through a high numerical aperture (NA) converging lens, is employed to create a trap that is created by opposing components of the scattering forces and gradient forces without using any non-optical forces like gravity. Figure 1.1(b) shows a schematic of a single beam optical trap formed using a high numerical aperture (NA) converging lens. The purpose of high NA converging lens is to create a high intensity gradient at the focus of converging lens, thereby exceeding the effect of the scattering force, which results in creation of a stable three dimensional trap at the lens focus, as shown in Figure 1.1(b). The single beam optical trap instrument is now widely known as optical tweezers.

The unique abilities of the single beam optical trap have had revolutionary impact in various subfields of sciences where single particles play a role. In atomic physics, laser trapping and cooling have resulted in the ability to trap single atoms [9]. The ability of optical tweezers to exert and measure molecular scale forces has led to exciting understanding of motor molecules. The first experiments involving live material using optical tweezers was the trapping of bacteria and viruses reported in [10]. The optical tweezers setup is now employed as a primary tool for single molecule research. With its femto-Newton force resolution and a spatial resolution of less than ten nanometers at milli-second time scales, it has become possible to study the dynamics of motor proteins, such as Myosin, Kinesin and Dynein. Motor proteins are proteins that exhibit locomotion along polymeric tracks like the Actin filament or microtubules, in the presence of energy molecules such as Adenosine Tri-Phosphate (ATP). Myosin is responsible for muscle contraction and vesicle transport within the cell for cellular pusposes. Kinesin and Dynein on the other hand also contribute to transport of cell

cargo called vesicles and for separation of chromosomes during cell divisions. Optical tweezers have been used to measure the step size of Myosin during its walk over Actin filament [11, 12, 13, 14, 15, 16] and of Kinesin during its walk over microtubules [17, 18, 19, 20, 21]. Apart from the step size measurement of Kinesin motor, there has been extensive study of the force dynamics of Kinesin molecule using optical tweezers. The load dependence on Kinesin motility was studied in [22], whilst the dynamics of force generation by a single Kinesin molecule were studied in [23, 24]. In [25], Endow et al presented their observation that certain mutants of Kinesin protein are capable of bi-directional movement on microtubules. Using optical tweezers there have been other works to study the mechanical rigidity of polymeric tracks for these motor proteins, namely microtubules and Actin filament [26, 27]. The locomotion of another kind of motor protein called Dynein was studied in [28, 29]. Optical tweezers have also been extensively used for DNA stretching studies where the two ends of a DNA strand are chemically tethered to microscopic polymer beads that are held in optical traps. The forces involved in DNA processes are then studied via the trapped beads by measuring the bead position [30, 31, 32, 7, 33]. In addition, optical tweezers has found use in numerous other cell biology applications involving intracellular materials like organelles and chromosomes [34, 35, 36].

The majority of optical tweezers setups are based on a single beam optical trap as shown in Figure 1.1. There are, however, alternate designs of trapping microscopic particles using the radiation pressure of light such as the counter-propagating traps using a dual beam of light and the Evanescent field tweezers. A simplistic schematic of dual beam based counter propagating optical tweezers [37, 38] is shown in Figure 1.2(a), where the two opposing light beams balance the scattering force component due to either beams. The trapping force along the transverse direction, as in the case of single beam optical tweezers, is provided by the gradient force. The Evanescent field optical tweezers use the Evanescent waves to trap dielectric particles. The Evanescent wave based optical tweezers is also called near field optical tweezers, because the intensity of Evanescent waves reduces exponentially with distance. A schematic showing Evanescent field tweezers is shown in Figure 1.2(b), where Evanescent waves are created when the angle of incident is beyond the critical angle resulting in total internal reflection. The residual waves that get transmitted are the evanescent waves that have

been demonstrated to create stable optical traps [39]. The evanescent field tweezers can manipulate particles upto a distance of 100 nm from the surface.

A more advanced optical tweezer setup can trap and manipulate multiple particles simultaneously [40] that can be achieved by manipulating a single laser beam by multiplexing in temporal or spatial domain. The time multiplexed traps can be created by using a fast actuator based on diffraction optics such as an acusto optic deflector or an electro optic deflector or rotating of the trapping beam using tip tilt mirrors. These actuators change the angle of incidence of trapping beam, thereby changing the position of optical trap in the focal plane. The time constant of beam switching between various locations is much faster than the time constant of an optical trap and that permits creating multiple traps by time multiplexing. Multiple traps are sometimes formed by spatial multiplexing, where a single trapping is beam is split into two or several stationary beams using a diffractive optic element like spatial light modulator (SLM) [41] or by using a polarizing beam splitter [42].

The requirements for biological assays necessitated the need for fast detection of trapped bead position in the optical tweezers setup, through which measurements on the bio-molecule under study are made. The initial setups used video based imaging [43] of trapped microscopic particles, which provided a temporal resolution of a few Hertz. Advancements in optical tweezers instrumentation, based on silicon based detectors [12, 14, 44], viz. four quadrant photodiode or dual-axis position sensitive photodiode, enabled millisecond temporal resolution and sub-nanometer spatial resolution. The photodiode based method measures the trapped particles position by directly imaging it onto the surface of a quadrant photodiode or position sensitive photodiode, after magnification. The most sensitive detection scheme for measuring the trapped bead position employs interferometric technique [40], where the trapping beam is passed through a Wollaston prism creating two physically displaced orthogonal polarizations. The two non-interfering beams pass through the sample, which contains the polymer bead to be trapped, and then recombined using another Wollaston prism. The polarization state of the combined beam gives a measure of bead position. This method however is of limited use as it provides position measurement only along one axis in the transverse plane. These advancements in optical tweezers instrumentation have led to exciting single cell single molecule studies for various biological systems by tethering them to

micron sized beads as handles [5].

The introduction of feedback strategies based on enhanced sensing due to photodetectors and fast actuation using AOD or EOD has led to further improvement in using optical tweezers as a force probe and measuring displacements in bio-assays. Feedback enhanced optical tweezer has played a pivotal role in instrumentation progress for higher resolution and higher bandwidth interrogation. Ashkin the inventor of optical tweezers used feedback in the optical levitation experiments [45], where the position of the levitated particle was sensed using a photodiode and a reference position was maintained by modulating the laser power. Here, the control signal gave a measure of the electric forces on oil drops thereby measuring single electron change accumulation. More feedback strategies have been used in optical tweezers to create constant position trap, also called the isometric clamp and constant force trap, also known as the isotonic clamp. In a constant position trap, the position of the trapped bead is maintained constant by regulating the trap position using a fast actuator, like an AOD. Finer [12] reported that by using the control signal (the regulating force), in a constant position feedback, as the measure of the externally applied force a pico-newton force resolution can be obtained with a milli-second time response. Constant position feedback enhanced optical tweezer results in an effective increase in the trap stiffness that is useful in reducing the effect of thermal noise on the trapped particle without increasing the laser power. The constant force feedback [20] involves maintaining a constant load on the trapped particle by maintaining a constant distance between the trap and the trapped bead. Therefore a constant force optical tweezer becomes particularly useful in measuring the locomotive steps (of a few nanometers) of motor proteins at constant load conditions. These feedback schemes are used in in-vitro studies of motor protein dynamics (kinesin [46], myosin [12]) and understanding the processes involving nucleic acids [32, 7] (stall forces in RNA, DNA transcription and translation).

However, these assays require slow process dynamics [12] (time constants in tens of milliseconds) to estimate the discrete steps of motor movements or the force dynamics, which is achieved by maintaining low ATP concentration in the buffer [12, 47] and limiting the number of adsorbed motor molecules [12] on the bead being used as a handle. At higher concentrations, motor movement along microtubule appears continuous,

that does not agree with the postulated discrete steps taken by the protein. A quantitative interpretation of forces experienced at higher resolution and higher bandwidth still remains a challenge [48, 49, 50] for the next generation of optical tweezers. The implementation of constant position optical tweezers using classical linear feedback and using the feedback signal as a measure of external force [14] limits the force estimation bandwidth of feedback enhanced optical tweezers. This research work is an attempt to address these questions by understanding the behavior of a constant position optical tweezers.

To this end, individual components of constant position optical tweezers are independently characterized using a system theoretic approach. Previously, there have been studies to investigate optical tweezers setup from a control systems perspective [51, 52]. In [51] comparisons based on simulations between the performance of constant position optical tweezers based on proportional control, LQG control, and nonlinear control strategies to reduce the effective Brownian motion were presented. Feedback enhanced tweezers based on integral control in a constant position setup, at lower frequencies, were studied in [52]. However, both these works lack in characterizing the trap dynamics at higher frequencies in closed loop setting and are inadequate in explaining some of the unexplained higher frequency anomalies that limit the optical tweezers bandwidth as a force probe. This work presents the reasons for the unexpected high frequency behavior of constant position optical tweezers by accounting for system latencies. The fundamental limitations that limit the force probe bandwidth of an optical tweezers setup are explained analytically and modern controls approach is employed that significantly improves the ability of optical tweezers to reliably measure external forces having high frequency content. It should be noted that the work presented in this dissertation makes no attempt to investigate optical tweezers from an optics viewpoint. Instead, a control systems framework is presented that provides an alternate paradigm to study optical tweezers.

1.1 Organization of Dissertation

The physics behind trapping of a microscopic particle using light is presented in Chapter 2. This gives a picture of the light forces in play behind optical tweezers.

In Chapter 3 a complete description of the experimental setup of optical tweezers system is presented. This chapter describes the various components, viz. laser, optics, sensing, actuation, data acquisition and controller, that are assembled for constant position optical tweezers operation.

For small displacements (upto roughly 200 nm) of the trapped particle from the center of the trap, optical tweezers behave as a Hookeian spring [53] characterized by a trap stiffness, k. This phenomological model is explained in detail in Chapter 4. The conventional methods in optical tweezers literature to characterize optical tweezers system are presented along with experimental results. In this chapter, a system theoretic model of optical tweezers along with block diagram schematics is developed and an input-output method of system identification is introduced to individually characterize various components of optical tweezers system. The results obtained using input-output method of system identification are found to be in good agreement with the anomalous pattern, i.e. emergence of peak, observed in the thermal noise power spectrum of trapped bead, as feedback gains are increased. The emergence of peaks in the thermal noise power spectrum is explained in terms of system latencies which imposes a fundamental limitation in using the feedback signal as a measure of external force with high frequency content. This limitation is explained using the second waterbed formula and an analytical expression is presented. Further, we analyze fundamental limitations on the achievable bandwidth using constant position feedback and maximum proportional feedback gains beyond which the system becomes unstable.

Chapter 5 and Chapter 6 address the question of increasing the force probe bandwidth of constant position optical tweezers. In Chapter 5, the external force to be measured is treated as a disturbance signal and a classical control systems approach is employed where an accurately characterized plant is inverted to estimate the disturbance signal. The efficacy of this approach is shown by comparing the experimental results obtained using this scheme with experimental results obtained using the conventional method of force estimation in optical tweezers. Chapter 6 further improves upon the results obtained using an ad-hoc approach of system inversion in Chapter 5 by casting the problem of external force estimation in a robust control framework. In the robust control paradigm, the performance objectives of a constant position optical tweezers are identified and appropriate weighting functions are designed to synthesize an

optimal control strategy over the space of all linear stabilizing controllers. The analytical and experimental results are presented to demonstrate the improvement of robust control strategy over system inversion approach.

Chapter 7 summarizes the targets achieved in this dissertation and discusses the future scope of this work.

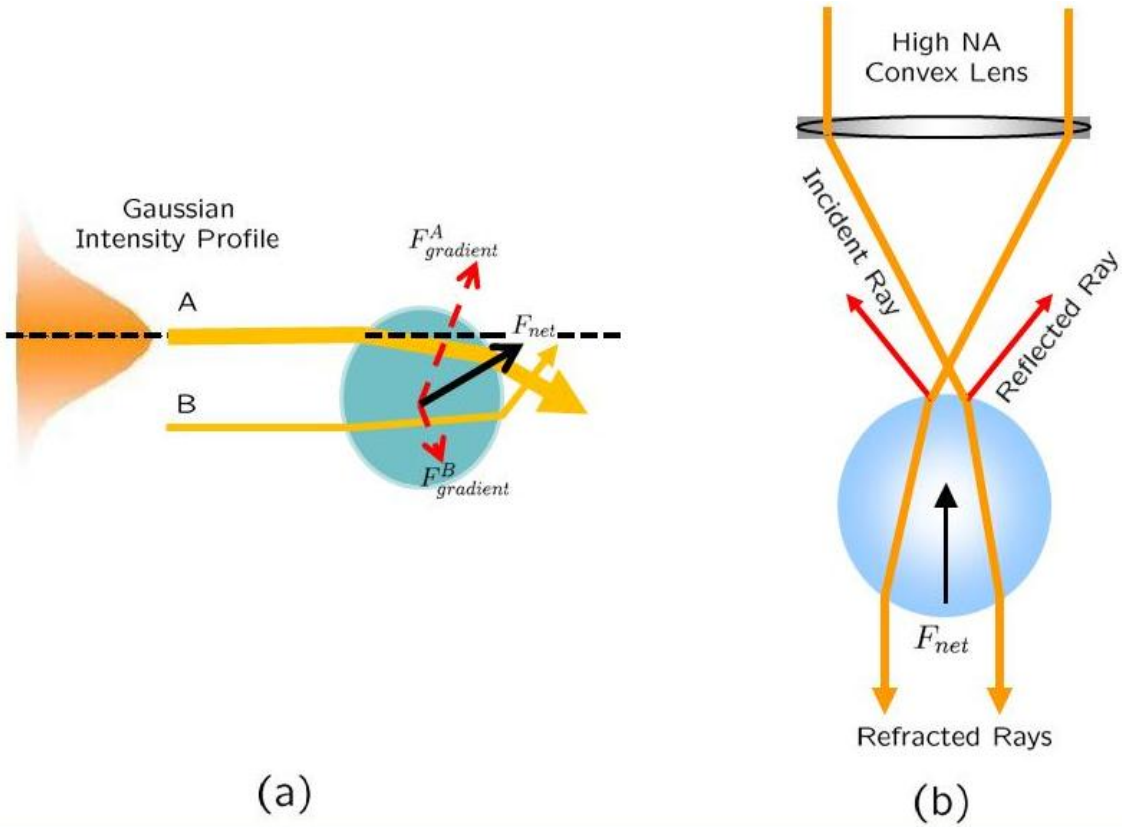

Figure 1.1: (a) This figure shows the gradient and scattering forces due to two light rays A and B on a microsphere. The light source has a Gaussian intensity profile with ray A having higher intensity than ray B. $F^A_{gradient}$ and $F^B_{gradient}$ are the gradient forces due to rays A and B respectively and F_{net} is the resultant gradient force on the microsphere due to $F^A_{gradient}$ and $F^B_{gradient}$. (b) This figure gives a qualitative picture when two light rays A and B passing through a high numerical aperture convex lens impinge on a microsphere that is located on the axial axis of the lens. The direction of incident, reflected and refracted rays is shown along with the net force F_{net}.

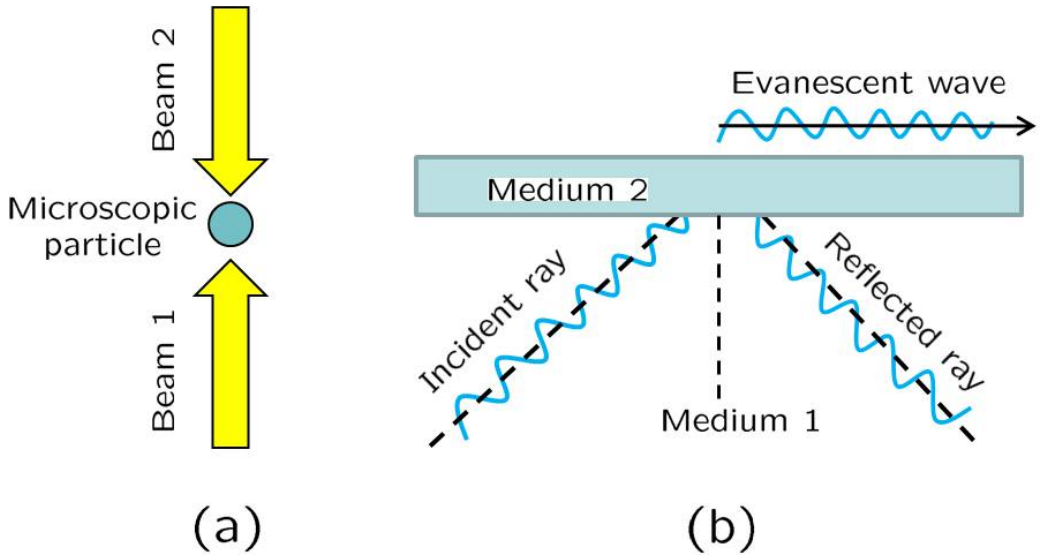

Figure 1.2: (a) This figure shows a simplistic view of an optical trap formed by two counter-propagating light beams in opposite direction. (b) This figure shows a qualitative picture of an optical trap formed due to the residual evanescent field waves. The angle of incidence should be above the critical angle for total internal reflection and formation of evanescent waves.

Chapter 2

PHYSICS OF AN OPTICAL TRAP

Light exerts radiation pressure on particles in its path. The radiation pressure of light is classified into two components - the scattering force and the gradient force. The scattering force acts in the direction of propagation of light and has a destabilizing effect for optical trapping of particles. On the other hand, the gradient force has a stabilizing effect and acts in the direction of intensity gradient of light. This chapter explains the phenomenon of optical trapping of microscopic particles based on the laws of physics and provides an insight into optical trapping. This analysis based on laws of physics helps build an intuition of the optical forces in play. However, such a model is of little use for measuring forces or displacement in bio-assays or other practical applications that require measurement in real time. A spring mass damper model presented in Chapter 4 is used for real time studies.

The analysis of optical forces, exerted on a particle in the path of light, differs - depending on the size of the particle and the wavelength of light. A particle having dimensions much smaller than the wavelength of light is considered to be in the Rayleigh regime, where the particle is assumed to be an electric dipole in an electro-magnetic field. If the particle size is much bigger than the wavelength of light, the ray optics analysis is done to study the effect of light. The analysis in this case is said to be in the Mie regime or ray optics regime. When the particle size is of the same order as the

wavelength of light, the analysis is said to be in the intermediate regime. Most of the optical trapping, done for bio-assays is done in intermediate regime.

This chapter presents physics based force analysis of optical trapping for particles in Rayleigh regime and Mie regime. The accurate modeling of forces in the intermediate regime requires solving the time dependent Maxwell equations with appropriate boundary conditions and is not discussed here. For a particle in the Rayleigh regime, optical trapping is explained in Section 2.1. The force analysis based on ray optics that explains the stability of an optical trap when the particle to be trapped is in the Mie regime is presented in Section 2.2.

2.1 Rayleigh regime analysis

When the size of particle is much smaller than the wavelength of light that impinges on it - the method of studying forces on the particle involves treating the particle as an electric dipole in an inhomogeneous electro-magnetic field. The force, F, applied on a single charge in an EM field is the Lorentz force, given by

$$\vec{F} = q\left(\vec{E} + \frac{d\vec{x}}{dt} \times \vec{B}\right), \tag{2.1}$$

where q is the charge on the electric mono-pole, $\vec{E}$ is the electric field vector at position $\vec{x}$ and $\vec{B}$ is the magnetic field vector at position, $\vec{x}$. The net force, F_{net} on the electric dipole can be written in terms of Lorentz force as

$$\vec{F}_{net} = q\left(\vec{E_1} - \vec{E_2} + \frac{d(\vec{x_1} - \vec{x_2})}{dt} \times \vec{B}\right), \tag{2.2}$$

where $\vec{E_1}$ and $\vec{E_2}$ are electric field vectors at positions of two electric charges of the electric dipole. The relation between $\vec{E_1}$ and $\vec{E_2}$ is $\vec{E_2} = \vec{E_1} + ((x_2 - x_1).\nabla)\vec{E}$. Define polarization, $\vec{P} = q\vec{d}$, where $\vec{d} = \vec{x_1} - \vec{x_2}$. The net force, F_{net}, can thus be expressed as,

$$\begin{aligned} \vec{F}_{net} &= q\left((\vec{d}.\nabla)\vec{E} + \frac{d(\vec{x_1} - \vec{x_2})}{dt} \times \vec{B}\right) \\ &= (\vec{P}.\nabla)\vec{E} + \frac{d\vec{P}}{dt} \times \vec{B} \\ &= \alpha\left((\vec{E}.\nabla)\vec{E} + \frac{d\vec{E}}{dt} \times \vec{B}\right), \end{aligned} \tag{2.3}$$

for a linear dielectric particle, i.e. $\vec{P} = \alpha\vec{E}$. Using Maxwell's equation, $(\vec{E}.\nabla)\vec{E} = \frac{1}{2}\nabla\vec{E}^2 - \vec{E} \times \left(-\frac{d\vec{B}}{dt}\right)$, (2.3) becomes

$$\begin{aligned} \vec{F}_{net} &= \alpha\left(\frac{1}{2}\nabla\vec{E}^2 + \vec{E} \times \frac{d\vec{B}}{dt} + \frac{d\vec{E}}{dt} \times \vec{B}\right) \\ &= \alpha\left(\frac{1}{2}\nabla\vec{E}^2 + \frac{d(\vec{E} \times \vec{B})}{dt}\right). \end{aligned} \tag{2.4}$$

The term $\frac{d(\vec{E}\times\vec{B})}{dt}$ is the time derivative of Poynting vector, which describes the power per unit area passing through a surface. For constant laser power, the Poynting vector is constant. Therefore,

$$\vec{F}_{net} = \alpha\left(\frac{1}{2}\nabla\vec{E}^2\right). \tag{2.5}$$

The term $\vec{E}^2$ is the square of electric field vector, and thus is the intensity of the beam as a function of position. The net force is thus proportional to the gradient along the intensity of the beam, i.e. the particle is attracted to the region of highest intensity. In reality, scattering force acts towards the direction of light propagation and an equilibrium position is attained slightly downstream of intensity maximum.

2.2 Mie regime analysis

The figures and proofs presented here are taken from [54]. The geometry for calculating the force due to the scattering of a single incident ray, KA, of power P by a dielectric sphere (centered at O) is shown in Figure 2.1. PR is the ray reflected at the outer surface of the sphere and an infinite set of internally refracted rays are denoted by PT^2R^n, where R and T are the reflection and transmission coefficients of the surface, with $R+T = 1$ and n is the number of times a particular ray has got reflected. The index of refraction for the incident medium is n_1 and for the dielectric is n_2. The incident ray, KA, has power P and is assumed to be along the positive Z-axis with the angle of incidence, $\angle KAL$, being θ and the angle of refraction, $\angle OAB$, be r. The force, F, of the incident ray is

$$F = \frac{n_1 P}{c},$$

where c is the velocity of light. The power of first reflected ray by PR, the first transmitted ray, AB, has power PT, The second transmitted ray, BH, has power PT^2, the ray BC has gone transmitted once and reflected once and has a power PTR and so on. In $\triangle OAB$

$$\angle OAB = \angle OBA = r.$$

Let the transmitted ray BH make an angle α with the positive Z axis. Therefore,

$$\begin{aligned} \alpha &= \angle HFM \\ &= \angle BAF + \angle BFA \\ &= 2(\theta - r). \end{aligned}$$

Using the Snell's law of refraction ($n_{incidence} Sin(\theta_{incidence}) = n_{refraction} Sin(\theta_{refraction})$),

$$\angle HBC = \pi - (r + \theta).$$

Let the transmitted ray CN make an angle β with the ray BH, i.e. $\angle IHC = \beta$, therefore

$$\begin{aligned} \beta &= \angle HBC + \angle BCH \\ &= \pi - (r + \theta) + (\theta - r) \\ &= \pi - 2r. \end{aligned}$$

The transmitted ray CN thus makes an angle $(\alpha+\beta)$ with the positive Z axis. Similarly it can be shown that every subsequent transmitted ray undergoes a rotation by an angle β with respect to its immediately previous transmitted ray. Therefore $\angle DNJ = \beta$ and the ray ND makes an angle $(\alpha + 2\beta)$ with the positive Z axis.

From the law of conservation of momentum, the net momentum (and momentum per unit time) of the incident ray is conserved. Momentum per unit time of the ray AE is $\frac{n_1 PR}{c}$. Its component in the positive Z direction is $\frac{n_1 PR}{c} Cos(\pi - 2\theta)$. The momentum per unit time along the Z axis for ray BH is $\frac{n_1 PT^2}{c} Cos(\alpha)$. Momentum per unit time along the Z axis for rays CN and ND is $\frac{n_1 PT^2 R}{c} Cos(\alpha + \beta)$ and $\frac{n_1 PT^2 R^2}{c} Cos(\alpha + 2\beta)$ respectively. Similarly, the momentum per unit time along the Z axis for the transmitted ray that has undergone reflection n times is $\frac{n_1 PT^2 R^n}{c} Cos(\alpha + n\beta)$. Therefore the net

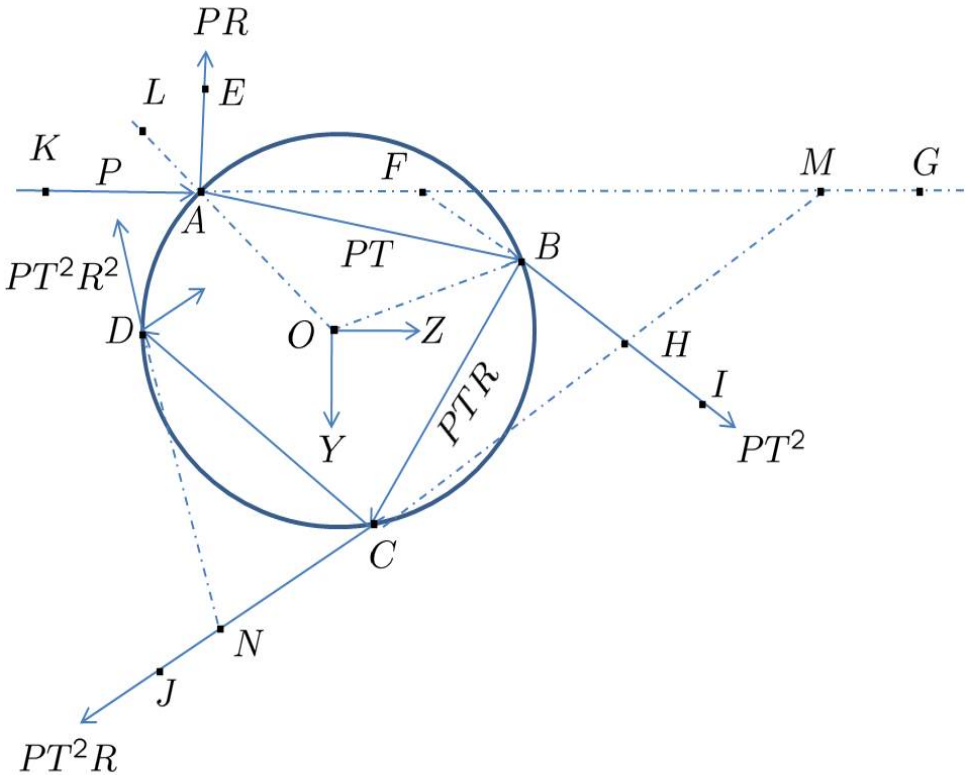

Figure 2.1: This figure shows the ray optics diagram for a ray KA, having power P, impinging on a sphere centered at O. The refractive index of the incident medium is n_1 and that of sphere is n_2. The reflectivity and transmissivity of the sphere is R and T respectively. The angle of incidence and refraction are θ and r respectively. This figure shows the original incident ray KA undergoing multiple reflection and refraction.

force experienced by the bead along the Z axis (called the scattering force, F_s) is

$$\begin{aligned} F_z &= \frac{n_1 P}{c} - \frac{n_1 P}{c} R\, Cos(\pi - 2\theta) + \frac{n_1 P}{c} T^2 Cos(\alpha) + \\ &\quad \frac{n_1 P}{c} T^2 R\, Cos(\alpha + \beta) + \frac{n_1 P}{c} T^2 R^2 Cos(\alpha + 2\beta) + \ldots \\ &= \frac{n_1 P}{c} + \frac{n_1 P}{c} R\, Cos(2\theta) - \frac{n_1 P}{c} T^2 \sum_{n=0}^{\infty} R^n Cos(\alpha + n\beta) \\ &= \frac{n_1 P}{c} \left[1 + R\, Cos(2\theta) - T^2 \sum_{n=0}^{\infty} R^n Cos(\alpha + n\beta) \right]. \end{aligned}$$

Similarly, balancing the forces along the Y axis yields the net force on the bead

along the Y axis (called the gradient force, F_g) as

$$F_y = \frac{n_1 P}{c}\left[R\ Sin(2\theta) - T^2 \sum_{n=0}^{\infty} R^n Sin(\alpha + n\beta)\right].$$

Note that $R \leq 1$, as it is the reflection coefficient, therefore taking the infinite sum yields

$$F_z = \frac{n_1 P}{c}(1 + R\ Cos(2\theta)) - \frac{n_1 P}{c} T^2 \frac{Cos(2(\theta - r)) + R\ Cos(2\theta)}{1 + R^2 + 2R\ Cos(2r)}, \quad (2.6)$$

$$\text{and } F_y = \frac{n_1 P}{c}\left[R\ Sin(2\theta) - T^2 \frac{Sin(2(\theta - r)) + R\ Sin(2\theta)}{1 + R^2 + 2R\ Cos(2r)}\right]. \quad (2.7)$$

The scattering and gradient force experienced by the spherical particle by a single ray are given by Equation 2.6 and Equation 2.7, respectively. The net force on the spherical particle due to the the whole beam is explained in the following sections.

2.3 Trap Focus along Z Axis

Consider the case when the center of spherical particle, O, lies on the geometric axis of the lens as shown in Figure 2.2 (a). The radius of the lens is r_{max} and the focus is denoted by f, that lies on the Z-axis. Consider a ray, $W'f$ in the plane $POWW'$ as shown in the Figure 2.2 (a). The plane $POWW'$ makes an angle β with the ZY plane. The ray $W'f$ makes an angle ϕ with the Z-axis and is at a distance r from the Z-axis before hitting the lens, i.e. $PW' = r$. Figure 2.2 (b) shows the same ray $W'f$ in the WZ plane. The scattering and gradient forces, F_s and F_g, due to the ray $W'f$ are shown and make an angle of ϕ and $90+\phi$, respectively, with the positive Z axis. The net effect of these forces due to the whole beam is the vector sum of scattering and gradient force contributions of all the individual rays and can be determined numerically. Qualitatively, it can be seen that because of symmetry the net force is axial as the transverse component of both gradient and scattering forces is balanced by an equal contribution from a ray located diametrically opposite. The components of gradient and scattering forces along the Z-axis are

$$F_s\ Cos\ \phi \text{ and } F_g\ Sin\ \phi.$$

The position of the particle center, O, relative to the focus, f, determines if the cumulative axial force acts towards the focus (a stable trap) or away from the focus (which

results in scattering of the particle).

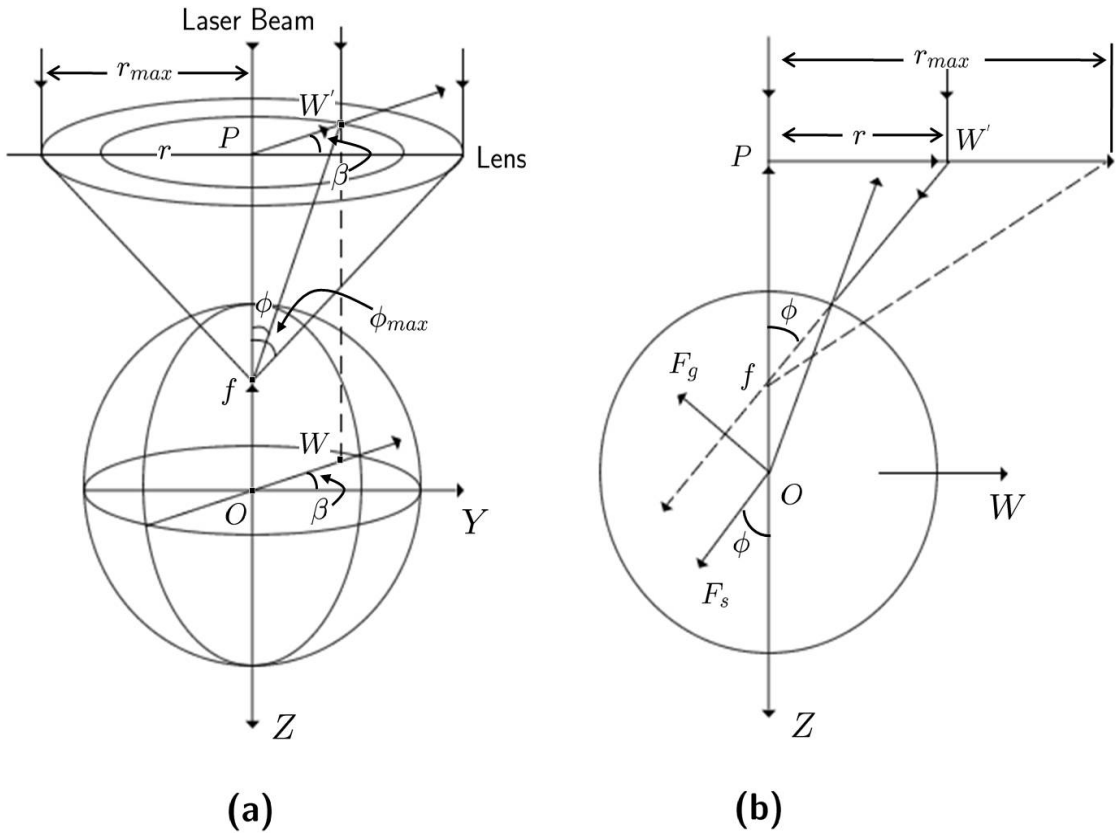

Figure 2.2: (a) Ray optics diagram when the spherical particle is located along the principal axis of lens. (b) This figure shows the ray optics configuration in the plane $OWW'P$.

2.4 Trap Focus along Y Axis

Consider the case when the center of spherical particle, O, lies on the transverse axis (say Y-axis) of the lens as shown in Figure 2.3 (a). Consider the incident ray Wf, that lies in the plane $AWW^{'}f$, which makes an angle β with the plane, ZY. The plane of incidence (which contains the incident ray and the normal, $\hat{n}$) is the plane containing the points O, f and V (V lies on the sphere) and is shown in Figure 2.3 (b). The incident ray, Wf makes an angle θ with the normal, $\hat{n}$. The distance of focus, f from

the center of the sphere, O, is $S^{'}$ and the ray hits the lens at a distance r from the center of the lens, i.e. $AW = r$. Bf is the projection of $fW^{'}$ on the Y-axis. In triangles $BVW^{'}$, OfV and $W^{'}fV$,

$$\begin{aligned} \angle BVW^{'} &= \mu, \\ \angle OfV &= \gamma \text{ and} \\ \angle W^{'}fV &= \alpha. \end{aligned}$$

In the Figure 2.3 (b),

$$\begin{aligned} R\ Sin\ \theta &= S^{'}\ Sin\ \gamma, \\ \text{which implies } Sin\ \theta &= S^{'}\ Sin\ \gamma, \text{ for } R = 1. \end{aligned} \tag{2.8}$$

Since $fW^{'}$ is the projection of fW on XY plane and fB is the projection of $fW^{'}$ on the Y-axis, therefore

$$\begin{aligned} fW^{'} &= fW\ Cos\ \alpha \text{ and} \\ fB &= fW^{'}\ Cos\ \beta. \end{aligned}$$

Also, fB is the projection of fW on the Y-axis, therefore

$$\begin{aligned} fB &= fW\ Cos\ \gamma, \\ \text{which implies } Cos\ \gamma &= Cos\ \alpha\ Cos\ \beta. \end{aligned} \tag{2.9}$$

Consider the plane $AWW^{'}f$. Let the coordinates of O, B, f, $W^{'}$, A and W in Figure 2.3 (a) be $(0,0,0)$, $(0, r\ Cos\ \beta - S^{'}, 0$, $(0, -S^{'}, 0)$, $(r\ Sin\ \beta, r\ Cos\ \beta - S^{'}, 0)$, $(0, -S^{'}, l)$ and $(r\ Sin\ \beta, r\ Cos\ \beta - S^{'}, l)$. Therefore $\vec{Af} = l\hat{k}$ and $\vec{W^{'}f} = r\ Sin\ \beta\ \hat{i} + r\ Cos\ \beta\ \hat{j}$, where $\hat{i}$, $\hat{j}$ and $\hat{k}$ are unit vectors along X, Y and Z axis. The vector, $\vec{n_1}$, normal to the plane $AWW^{'}f$ is given by

$$\begin{aligned} \vec{n_1} &= \vec{AF} \times \vec{W^{'}f}, \\ \text{which implies } \vec{n_1} &= -rl\ Cos\ \beta\ \hat{i} + rl\ Sin\ \beta\ \hat{j}. \end{aligned} \tag{2.10}$$

In the incident plane $WVfOB$,

$$\begin{aligned} \vec{WB} &= r\ Sin\ \beta\ \hat{i} + l\hat{k}, \\ \vec{S^{'}} &= S^{'}\hat{j}. \end{aligned}$$

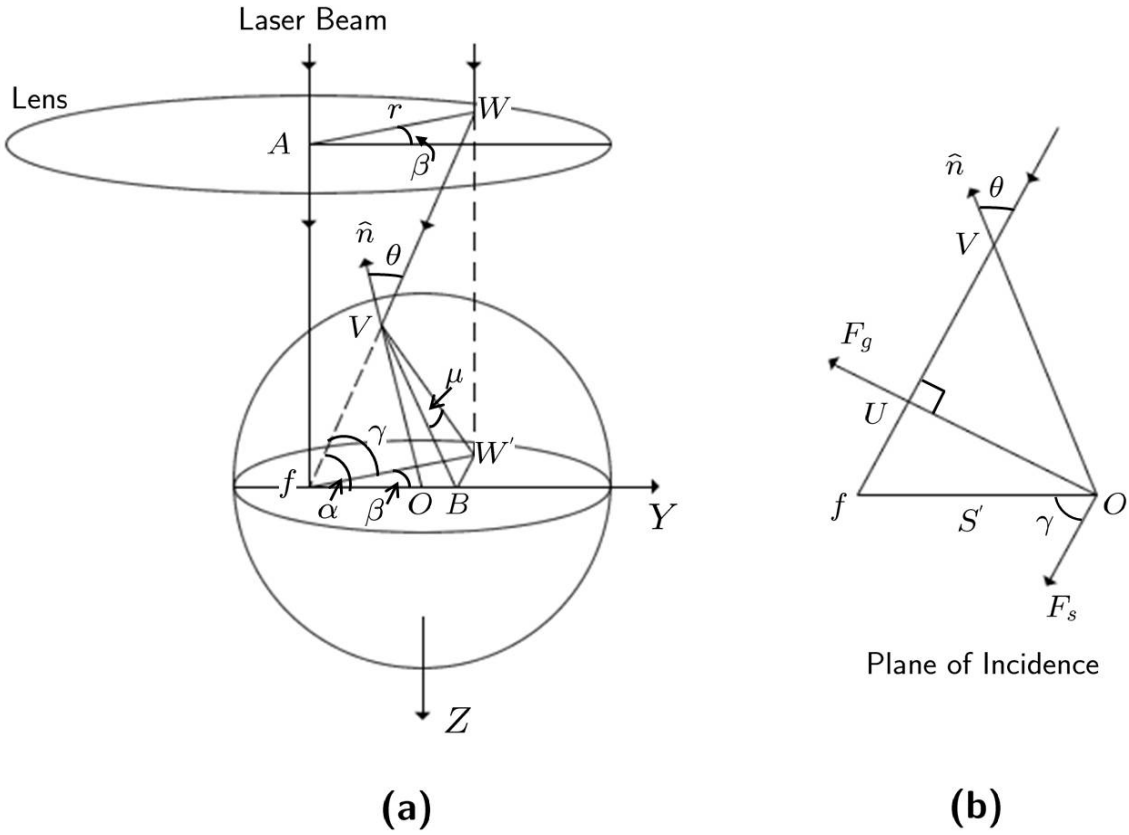

Figure 2.3: (a)Ray optics diagram when the spherical particle is located in the focal plane of the lens, but displaced from the principal axis. (b) This figure shows the configuration of rays in the plane of incidence.

Let $\hat{n_2}$ be perpendicular to the incident plane and defined as $\vec{WB} \times \vec{Of}$, therefore

$$\begin{aligned} \hat{n_2} &= -lS^{'}\hat{i} + rS^{'}\ Sin\ \beta\ \hat{k}, \\ \text{which implies } \hat{n_1}.\hat{n_2} &= rl^2S^{'}\ Cos\ \beta. \end{aligned} \tag{2.11}$$

The angle between the planes $AWW^{'}f$ and the incident plane $WVfOB$ is μ. Therefore,

$$\begin{aligned} Cos\ \mu &= \frac{rl^2S^{'}\ Cos\ \beta}{\sqrt{r^2l^2Cos^2\beta + r^2l^2Sin^2\beta}.\sqrt{r^2S^{'2}Sin^2\beta + l^2S^{'2}}}, \\ &= \frac{l\ Cos\ \gamma}{WB\ Cos\ \alpha}, \\ &= \frac{l}{fW^{'}}.\frac{fB}{WB}, \end{aligned}$$

$$\text{therefore } Cos\ \mu \;=\; \frac{tan\ \alpha}{tan\ \gamma}. \tag{2.12}$$

Unlike the case described in Sec. 2.3, in the present case the net force depends on the choice of input polarization. Assuming an incident beam polarized perpendicular to the Y-axis, the component of electric field parallel to the vertical plane is $E\ Sin\ \beta$, where E is the amplitude of the electric field. The component of electric field perpendicular to the vertical plane is $E\ Cos\ \beta$. Let f_p and f_s be the fractions of input power along the p and s (parallel and perpendicular) polarization. Then

$$f_p \;=\; (Sin\ \beta\ Cos\ \mu - Cos\ \beta\ Sin\ \mu)^2, \text{ and} \tag{2.13}$$

$$f_s \;=\; (Sin\ \beta\ Sin\ \mu + Cos\ \beta\ Cos\ \mu)^2. \tag{2.14}$$

If the polarization of the incident beam is parallel to Y-axis, then f_p and f_s reverse. Knowing θ, f_p and f_s, the gradient and scattering force contributions of both $p-$ and $s-$ polarizations are computed separately using the expressions for f_p and f_s and the results are added. Qualitatively, it can be seen that the net force acting on the sphere is along the Y-axis and the stability of trap depends on the distance $S^{'}$.

Any arbitrary position of the center of sphere with respect to the trap focus can be resolved in terms of the above two cases. A qualitative picture of the net force on the sphere due to two incident rays (ray a and ray b) located symmetrically about the lens, is shown in Figure 2.4 (a), (b) and (c). The center of the sphere, O, lie on the axial axis, i.e. Z-axis with O lying below and above f in in Figure 2.4 (a) and (b), respectively. Figure 2.4 (c) considers the case where the sphere center, O, lies on the transverse axis of the lens and the resulting force due to rays a and b acts towards the focus, f.

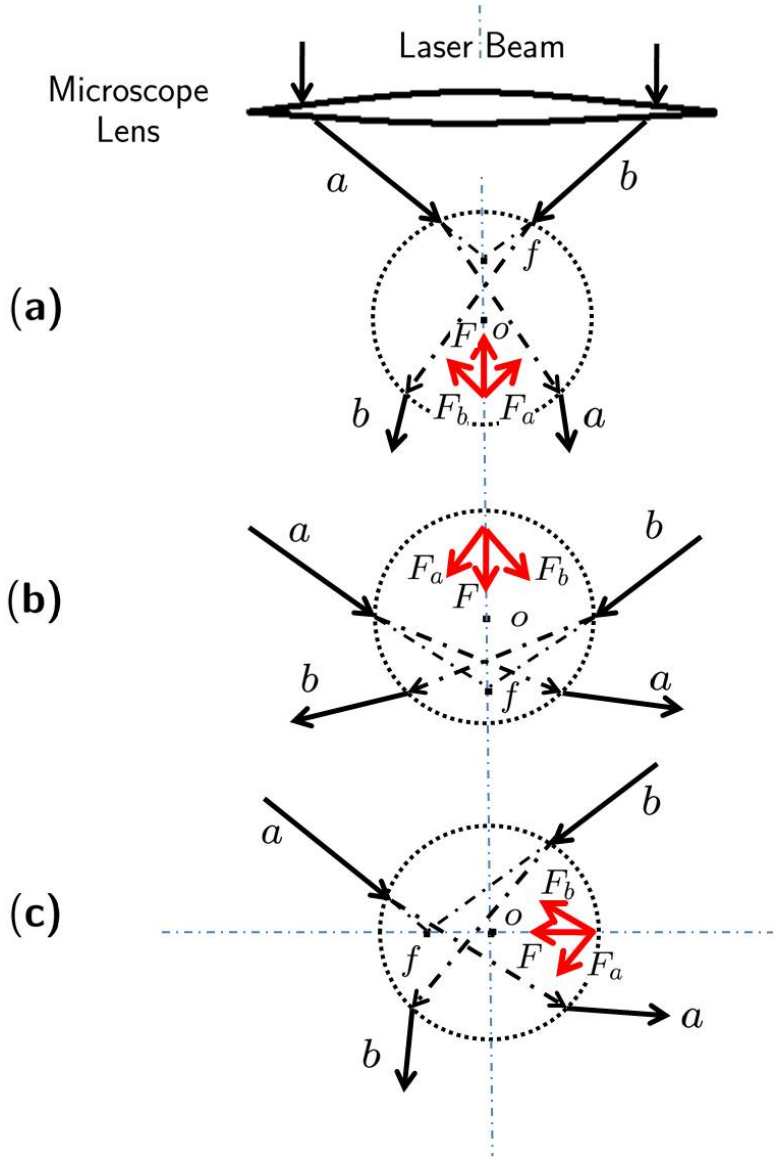

Figure 2.4: This figure shows the net force, due to scattering and gradient forces, acting on a microsphere in the path of light passing through a converging lens, when (a) microsphere is along the axial axis of lens with its center downstream of the focal point of lens; (b) microsphere is along the axial axis of lens with its center upstream of the focal point of lens; (c) the center of microsphere lies in the focal plane with but displaced from the principal axis of the lens.

Chapter 3

EXPERIMENTAL SETUP

Figure 3.1 shows the schematic of the optical tweezers setup along with the detection and feedback mechanism. A linearly polarized infrared laser beam from a continuous wave diode pumped Nd:YAG laser (CrystaLaser Inc., $\lambda = 1064$ nm, beam waist = 0.45 mm, maximum power output = 500 mW) is expanded using a $10\times$ beam expander (Thorlabs Inc.) and then passed through a half wave plate that modulates the angle of inclination of the linearly polarized light. A polarizing beam splitter cube ($PBS1$, Newport Inc.) allows the p-polarized component (shown in green color in Figure 3.1) of the laser beam to pass through and reflects the s-polarized component (shown in green color in Figure 3.1) at right angle, thereby creating two non interfering beams having different polarized states. The power in the p-polarized component is kept much lower than its s-polarized counterpart using the half wave plate. This is done primarily to use the s-polarized beam for creating the trap and have detection of the trapped particle's movement as the primary purpose of the weak p-polarized beam. The PBS should ideally allow the p-component to pass through while reflecting the whole of the s-component, however, approximately 4% of the p-component gets reflected and about 0.01% of the s-polarized beam goes through the beam splitter that results in a small amount of coupling between the two states. It is for the significantly lower leakage of s-polarized beam that p-polarized beam is used for detection. The s-polarized beam is passed through a dual Axis, acousto Optic Deflector, AOD (Intraction Corp. DTD-276HD6) and combined with the p-polarized beam at the second beam splitter $PBS2$. Both the p-pol and s-pol beams are passed through separate telescopic arrangement

of plano-convex lenses (not shown in the figure). The telescopic lenses in the s-pol beam path have properly matched focal lengths to make the input aperture of the AOD conjugate with the back focal plane of the microscope objective. Similarly the focal length of telescopic lenses in the p-pol beam path is chosen to have the back focal point of the first lens conjugate with the back aperture of microscope objective. The combined beam is introduced into the inverted microscope (Nikon Inc., TE2000U) from the epi-fluorescence port and directed into the back aperture of the oil immersion objective (numerical aperture, NA, = 1.4) using a dichroic mirror, $DM1$. The high

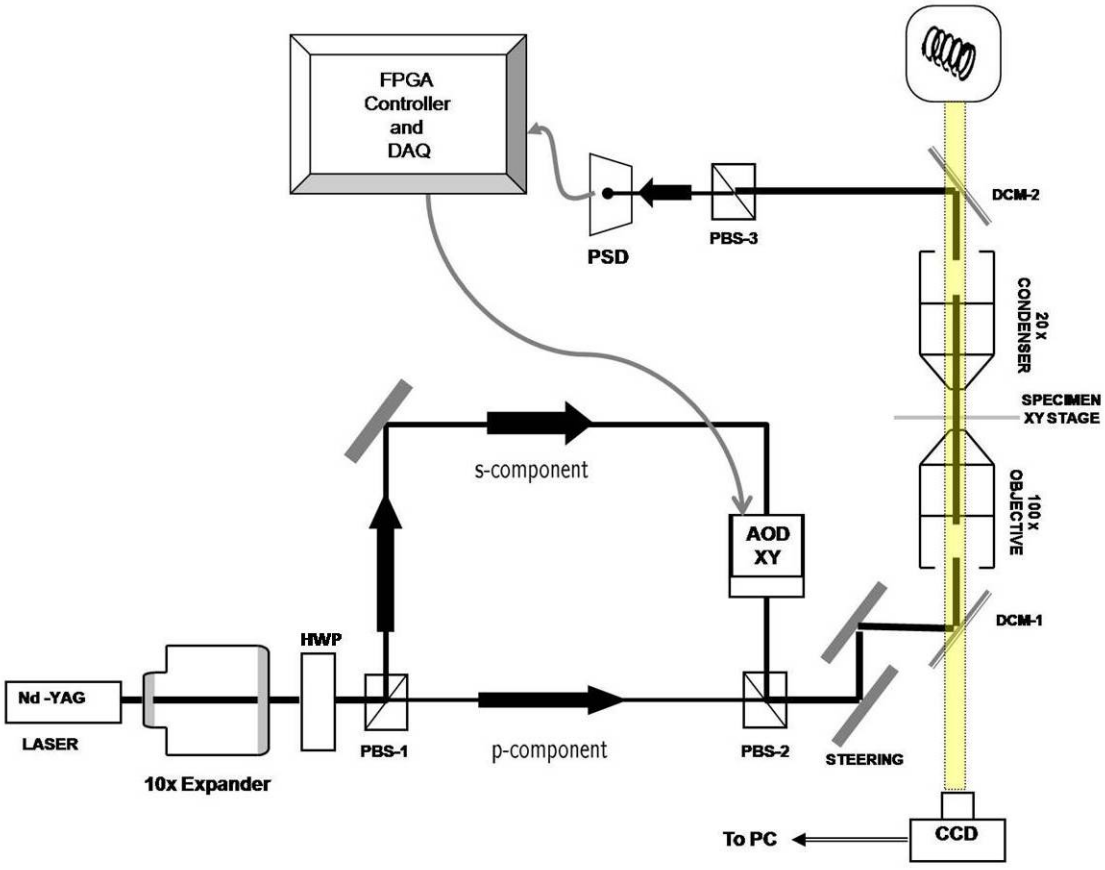

Figure 3.1: The figure shows the schematic of experimental setup of the Optical Tweezers system used in our laboratory.

NA objective converges the two beams to the image plane where it creates two optical trap centers inside the specimen. The specimen is a colloidal solution of, 1.1 μm or 2.1

μm in diameter, polystyrene beads (Bangs Labs Inc.). The specimen is mounted on a custom built, X-Y piezo-electric actuated, stage (Asylum Research), that can be moved manually or controlled through a computer.

The detection scheme consists of a condenser, a 20× objective, mounted above the sample stage on a manual X-Y-Z positioner. It provides illumination for the sample by focusing the light from the lamp above and collimates the diverging laser beam from below. The collimated beam is incident upon a third beam splitter $PBS3$ via dichroic mirror $DM2$. $PBS3$ splits the beam into p- and s- polarizations. The p-polarization is allowed to directly fall on a position sensitive photodetector, PSD (Pacific Silicon Sensor Inc., DL100-7PCBA3) while the high power s-polarized beam is collected in a beam dump (not shown in the figure). A FPGA based data acquisition system (National Instruments, PCI 7833R) is used to capture photodiode signals and implement a digital controller for feedback purpose, in real time. The controller output actuates the trap position by modulating the input to AOD. High frequency inputs to the tweezers is also introduced by modulating the trap position using the same AOD. This is done by adding the desired frequency input to the control signal in FPGA. A colored charged couple device, CCD, camera is used to view the specimen on the computer. The optical setup is mounted on an air table (Melles Griot Inc.) to isolate it from external mechanical vibrations. The detection system optics are mounted on a custom made aluminum optical breadboard.

The p-polarized component that is used as a detection beam only passes through static optics and thus converges to a constant point in the specimen plane through out the experiment. On the other hand, the s-polarized component of laser beam, which is used as the trapping beam passes through AOD which is a dynamic optical component. The position of trapping beam can be varied by modulating the AOD through the computer.

Chapter 4

Modeling and Characterization

The experimental setup for the optical tweezers was explained in Chapter 3 along with the detection and feedback mechanism [20, 42]. The next logical step is to use the optical tweezers setup for experiments requiring force and position measurements. Hence the need to understand the phenomological model and characterize the tweezer system.

4.1 Spring Mass Damper system

A qualitative picture of the net forces on the dielectric particle were presented in Chapter 2. It was shown that the total force on the particle in the trap acts towards the focus of the convergent lens (objective). Thus the radiation pressure force on the particle is restoring in nature and coupled with the damping of the fluid medium the particle is in, the tweezers system can be modeled as a spring mass damper system. It is observed experimentally that for small displacements of the bead or the dielectric particle from the center of the trap, optical tweezer behaves as a linear spring with a constant stiffness constant, k. However as the bead is displaced further away from the trap center, the restoring force changes non-linearly. As an example, a polystyrene bead of diameter, approximately, 1 μm in an optical trap formed using a laser of power 300-500 mW experiences a linear spring force upto a displacement of around 200 nm from the trap center.

Figure 4.1 shows a spring mass damper system. The equation of motion for this

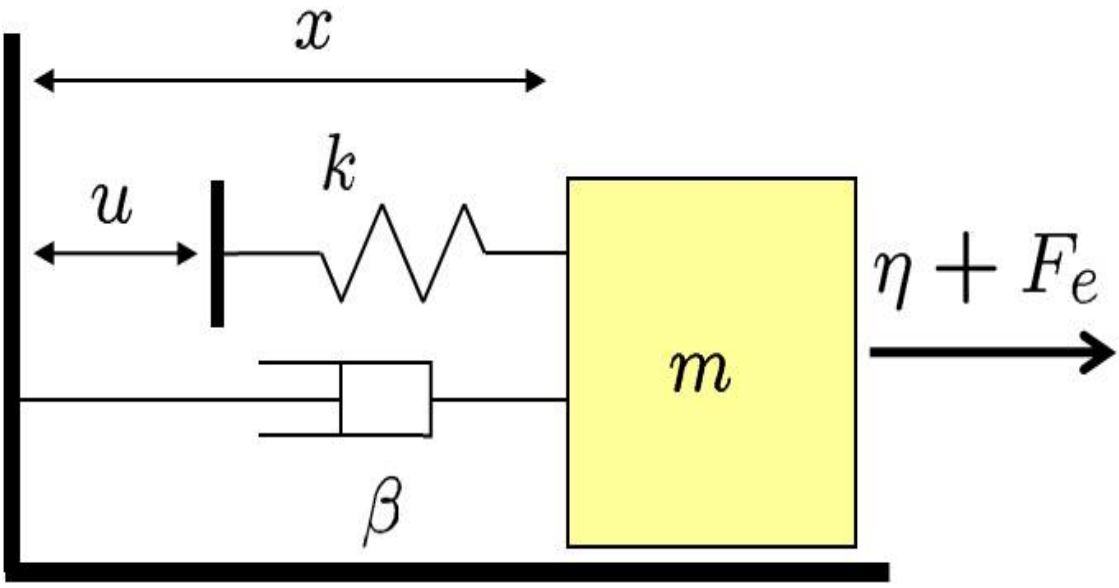

Figure 4.1: The figure on the left shows a spring mass damper system with a spring constant of k and damping coefficient of β and a mass m. The extension of the spring is $x - u$, where x is the absolute position of the mass, m, and u is the absolute position of the wall. The external forces on the mass are $\eta(t)$ and $F_e(t)$.

system is

$$m\ddot{x} + \beta\dot{x} + k(x - u) = \eta(t) + F(t), \tag{4.1}$$

where x is the absolute position of mass, m, u is the absolute position of the wall, $x - u$ is the extension of the spring and $\eta(t)$ and $F(t)$ are the external forces on the mass, m. The spring constant is denoted by k and the damping coefficient is denoted by β. (4.1) can be interpreted for an optical tweezers system as a bead of mass, m, in an optical trap with a linear trap stiffness, k, and a damping coefficient, β, arising due to the viscosity of the fluid medium. The instantaneous position of trapped bead is $x(t)$ and the instantaneous position of the trap is given by $u(t)$. The thermal force (also called the Langevin force) acting on the trapped bead due to absolute temperature is $\eta(t)$ and $F(t)$ is any other external force on the trapped bead.

Typical values of m, β and k are of the order of 10^{-15}, 10^{-8} and 10^{-5} in SI units respectively, making the system highly overdamped. The bead dynamics, hence, reduces

to a first order equation,

$$\beta\dot{x} + k(x - u) = \eta(t) + F(t). \tag{4.2}$$

4.2 Characterization and Calibration

The sensor used to measure bead movement is the photodiode (PSD in Figure 3.1), that collects laser beam refracted by the trapped bead and generates a voltage signal. The voltage signal magnitude is dependent on the position where the beam hits the

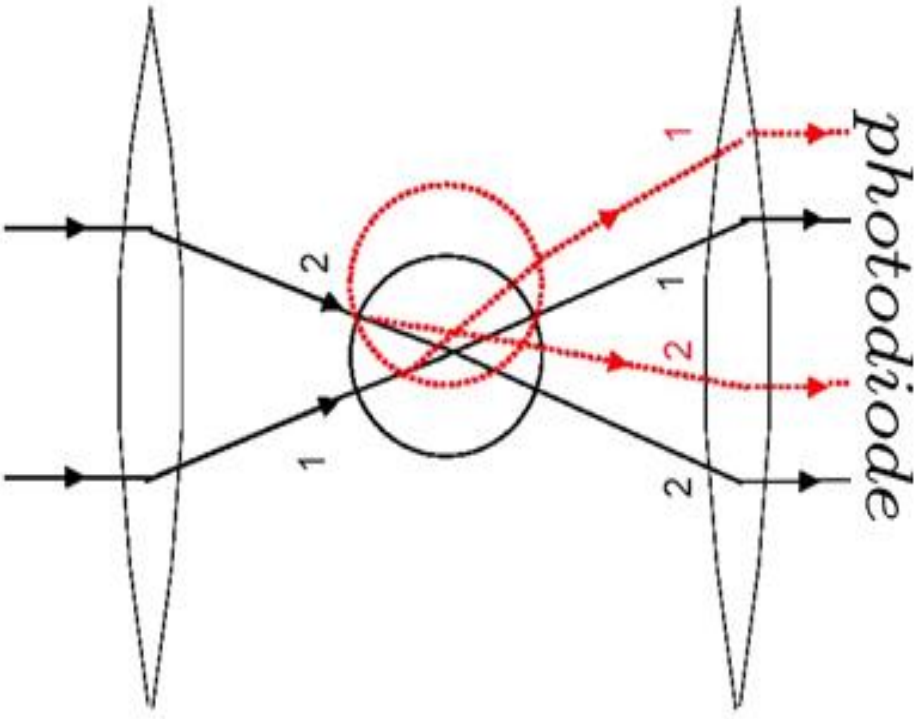

Figure 4.2: The figure shows change in position of two rays 1 and 2 passing through the bead and falling on the photodiode as the bead position changes.

photodiode. Figure 4.2 shows the change in the position of laser beam falling on the photodiode as the bead position changes. Therefore the photodiode voltage needs to be calibrated as a measure of bead movement. This quantity is referred to as photodiode sensitivity.

The photodiode sensitivity is determined by moving the trapped bead a known distance by moving the trap position using the AOD and the photodiode voltage measured. This requires AOD calibration to determine relationship between input to AOD and the change in the trap position (focused laser position in the specimen plane). The change in the position of trap center is viewed on a computer monitor using a CCD (charge couple device) camera. Thus, a mapping between distances on the specimen plane and on computer monitor needs to be accomplished. Therefore we need to calibrate

- computer screen,
- AOD and
- photodetector sensitivity.

4.2.1 Computer Screen

The computer screen is calibrated using a diamond ruled pre-calibrated slide. The conversion factor is determined by taking the ratio of measured distance between computer screen images of two diamond markers and the actual distance on the graduated diamond ruled slide. The distance on the computer screen between two graduated diamond lines on the calibrated slide, 52.5 μm apart is measured to be 26.25 cm. Thus a unity distance (in cm) on the computer screen refers to 2 μm on the specimen plane.

4.2.2 AOD

Once the computer screen is calibrated, AOD can be calibrated by applying a known input frequency (in MHz) and measuring the translation of focused laser spot position (trap position) on the computer screen. This procedure is repeated for several input frequencies and average of the laser spot displacement is taken. In our setup, the trap spot moved by 3 μm for a change in input frequency of 1 MHz.

4.2.3 Photodetector Sensitivity

The trapped bead is oscillated along a known distance in the transverse plane by actuating the trapping beam with the AOD, while the detection beam is kept stationary at the center. As the trapped bead moves, the deflection of detection beam falling on

the photodiode changes. This method of photodetector calibration offers the advantage of determining sensitivity for the bead to be used in the actual experiment. In our experiment, a triangular wave input is applied to the AOD in one of the axis, which drives the trap with a constant velocity in and out of the waist of the detection beam.

The S-shaped photodiode sensitivity curve obtained using this method is shown in Figure 4.3. The output is triangular if the displacement is within linear region of trap stiffness. The slope of this line (volts/time) divided by bead velocity (nm/time) gives photodiode sensitivity (volts/nm). From the sensitivity plot of photodiode in Figure 4.3, it can be seen that the detection scheme remains in the linear region for less than 500 nm displacement about the zero position.

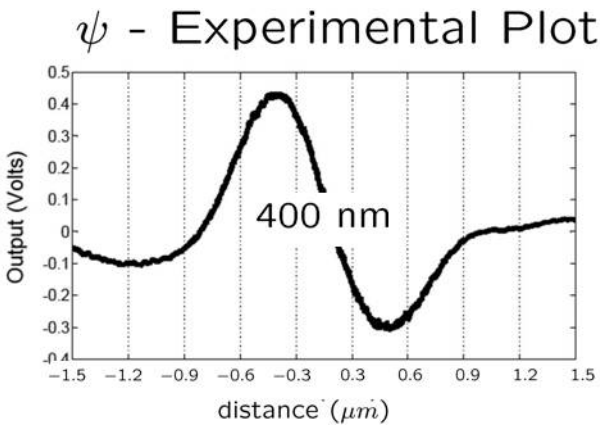

Figure 4.3: The figure shows plot of photodetector sensitivity with the photodetector output plotted on the Y-axis as the trapped bead is oscillated about the mean position at constant speed. The linear region of detection is approximately 200 nm about the zero position of the trap.

4.3 Optical Tweezers Modeling

The dynamics of a trapped bead can be expressed as first order differential equation as given in (4.2). From a systems viewpoint the (4.2) can be written as

$$\begin{aligned} X(s) &= k\frac{1}{\beta s + k}u(s) + \frac{1}{\beta s + k}(\eta(s) + F_e(s)), \\ X(s) &= kG(s)u + G(s)(\eta(s) + F_e(s)), \end{aligned} \tag{4.3}$$

where $G(s)$ represents the optical tweezer transfer function and is given by $\frac{1}{\beta s+k}$. The external force, $F_e(s)$, sees the same transfer function as thermal noise, $\eta(s)$.

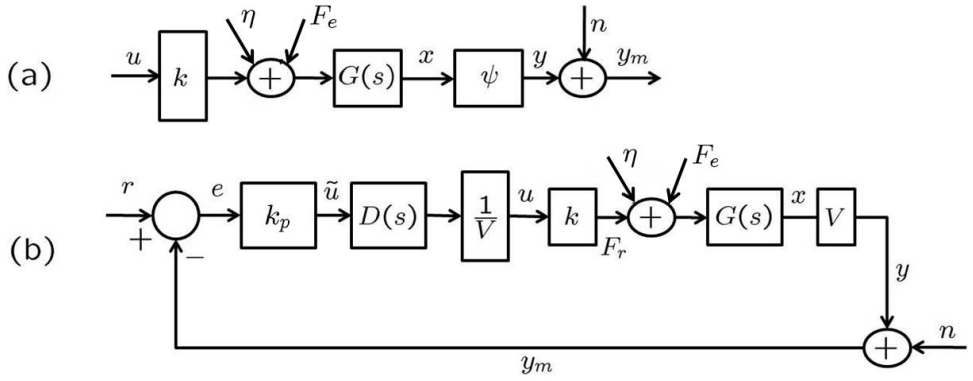

Figure 4.4: The figure shows the block diagram of optical tweezers system in (a) with η, F_e and u as inputs to the plant $G(s)$. x is the bead position, ψ is the map that provides the photodiode voltage for a given bead position and is nonlinear, n is measurement noise and y_m is photodiode output. (b) shows the block diagram of constant position optical tweezers with reference, r, kept at 0. V is the constant photodiode sensitivity in the linear region of operation.

Figure 4.4(a) shows the block diagram of tweezer system with plant transfer function G(s), trap stiffness k and thermal noise force, $\eta(t)$, external force, $F_e(t)$ and the trap position, $u(t)$ as the inputs to the plant. The block $\psi(s)$ is a non linear function that represents the sensitivity of the photodiode. Its units are mV/nm. However, for bead displacements of up to 300 nm from the trap center, linearity of the trap is assumed and ψ is a constant. Figure 4.4 (b) shows the block diagram of optical tweezers plant in a closed loop setting, with the goal of constant position regulation using a proportional controller with gain k_p. Here the nonlinear sensitivity is replaced by a constant, V, as the position feedback helps maintain the trapped bead in the linear region. The transfer function $D(s)$ accounts for the delays in the closed loop implementation and is explained in the next section. For analysis here, $D(s)$ is assumed to be unity. For the closed loop case, $u(s) = -k_p x(s)$, therefore,

$$\begin{aligned} X(s) &= \frac{G(s)}{1+G(s)kk_p}(\eta(s)+F_e(s)) - \frac{1}{V}k_pG(s)n(s), \\ X(s) &= \frac{1}{\beta s + k(1+k_p)}(\eta(s)+F_e(s)). \end{aligned} \tag{4.4}$$

Comparing with (4.3), the effective spring constant in the closed loop increases by a factor of $1 + k_p$, thereby better rejecting any disturbance. The closed loop bandwidth of the trap also increases by the same factor, $1 + k_p$.

4.3.1 Characterization based on Power Spectrum method

Characterizing the optical tweezer system requires estimating the trap stiffness, k. Various methods are reported, in literature [40], to calibrate the spring constant of the trap, like the equipartition method, the drag force method, the step response method and the method of power spectrum. The most popular, however, is the power spectrum method that involves evaluating the power spectrum of the photodiode output, y_m, in Figure 4.4(a). The power spectrum, $P_y(f)$ of the y is given as,

$$P_y(f) = V^2 \frac{k_B T}{\beta \pi^2 (f^2 + {f_c}^2)},$$

where k_B is the Boltzmann constant, T is the absolute temperature, $f_c = k/2\pi\beta$ is the cut off frequency of the trap and S is the sensitivity of the photodetector when operated in the linear region. By fitting a Lorentzian fit to the experimentally obtained power spectrum, the cut off frequency and therefore the trap stiffness is determined. This gives the plant transfer function, $G(s) = \frac{1}{\beta s + k}$, from (4.3).

4.3.2 Emergence of peak in Thermal Noise Spectrum

For the closed loop case with a proportional feedback gain, k_p, the effective trap stiffness, from (4.4), becomes $k(1 + k_p)$ and the closed loop transfer function between the input $(\eta + F_e)$ and the position of bead x is given by $G_{CL}(s) = \frac{1}{\beta s + k(1+k_p)}$ (assuming $D(s)$ is unity). Thus the cutoff frequency, in the closed loop case, is expected to increase linearly by a factor of $1 + k_p$. However, as the proportional gain is increased, emergence of a marked peak at higher frequencies is observed in the experimentally obtained power spectrum as shown in Figure 4.5 . This anomaly suggests a shift of the trap dynamics from a first order system to a higher order and can not be explained by the existing models, considered so far by the tweezers community. Also, it is observed that as gain is further increased the trap becomes unstable and the bead is lost. This is again in contrast with the hitherto assumed model that suggests the trapped particle can be arbitrarily stabilized with an increase in k_p.

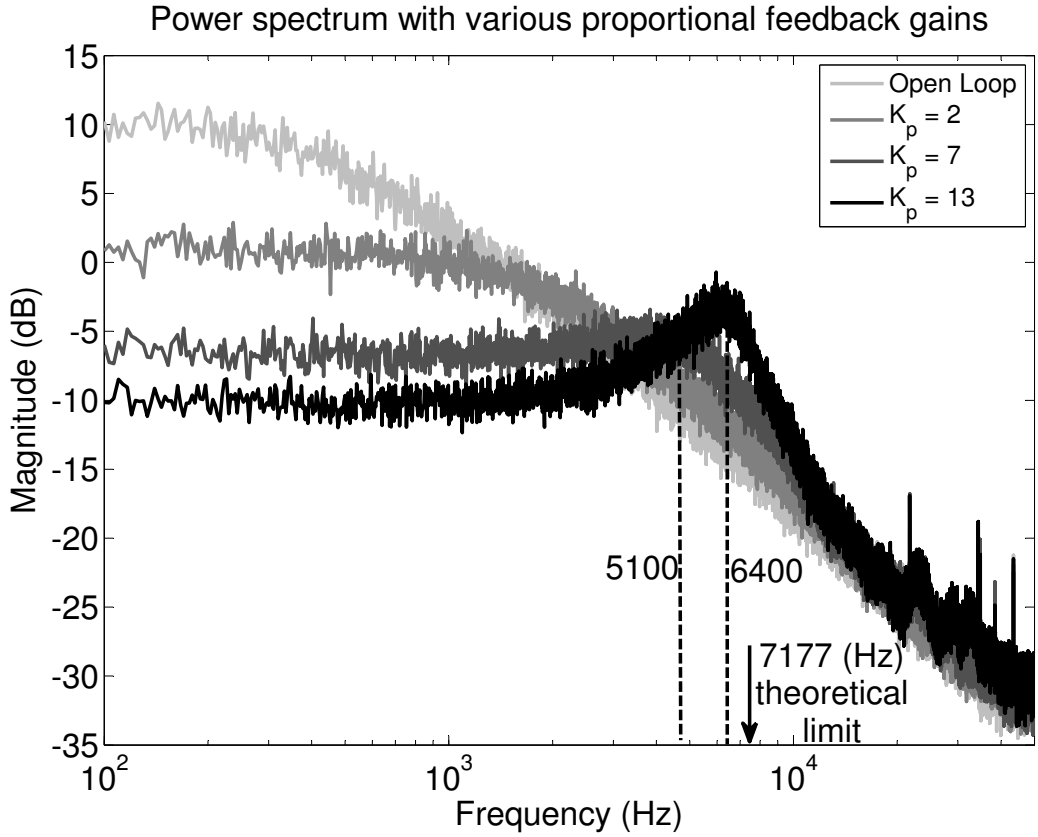

Figure 4.5: The figure shows thermal noise power spectrum of the photodetector output for a 2.1 μm diameter bead for different values of proportional gains, k_p, in a closed loop setting. As k_p is increased the trap becomes stiffer resulting in lower power at DC and shows emergence of peak.

As mentioned earlier in Section 4.1, optical tweezers is a highly overdamped system with a damping factor, ξ, given by

$$\xi = \frac{\beta}{\sqrt{2mk}},$$

where β, m and k are as given in (4.1). For a bead of diameter 2.1 μm and a trap of moderate open loop cut off frequency, f_c, of 500 Hz, the damping factor ξ evaluates to approximately 25, indicating a highly overdamped system. For the system to become critically damped, i.e. $\xi = 1$, the cut off frequency, f_c, of the trap should become 310 kHz, which corresponds to an increase in the trap stiffness of 620 times. Therefore,

for a value of k_p to be 619 the trap would become critically damped and the second order dynamics of the system would come into play. However from the experimentally obtained power spectrum, it is seen that the higher order effects come into play at moderate proportional gains of less than ten. Also, the frequency at which the peak is observed in the power spectrum is around 6 kHz. Therefore, the mass, m, playing a role in the bead dynamics does not explain the anomalous behavior.

4.3.3 Sampling Time and Delays

The cause of the higher order dynamics observed in the power spectrum, in the feedback enhanced optical tweezers can be traced to the presence of various latencies and delays in the feedback implementation. These delays get introduced due to the sampling time of the data acquisition system, the processing of acquired data by the controller and the actuator latencies, i.e. the AOD latency. The transfer function, $D(s)$, in Figure 4.4, can be approximated by the delay transfer function given by $exp(-(T_s + T_{AOD})s)$ where T_s is the FPGA delay due to data acquisition and execution of the controller code. T_{AOD} represents the AOD latency which is approximately 20 μs.

It is evident from the experimental power spectrum, that the feedback latencies impose a limit on the maximum closed loop bandwidth that can be achieved. Figure 4.6 shows the thermal power spectrum in the closed loop case with the proportional gain, k_p, set to 9 and four different cases of FPGA delay. As the closed loop latencies are reduced, the frequency at which the onset of peak begins shifts toward right to a higher value thereby resulting in higher bandwidth of the system.

In the feedback setup, modeling the various implementation delays explains the occurrence of peak in the thermal noise power spectrum. However, accounting for all the delays is an ad-hoc approach and requires a priori knowledge of the latencies involved. Also, the delay modeling depends on the kind of data acquisition implementation, eg. ADC sampling based on a zero order hold (ZOH) will need to be modeled differently from a first order hold implementation. In the following subsection, we present a frequency sweep based system identification approach applied to the tweezer setup that is particularly useful in the closed loop setup and does not require accounting for individual delays.

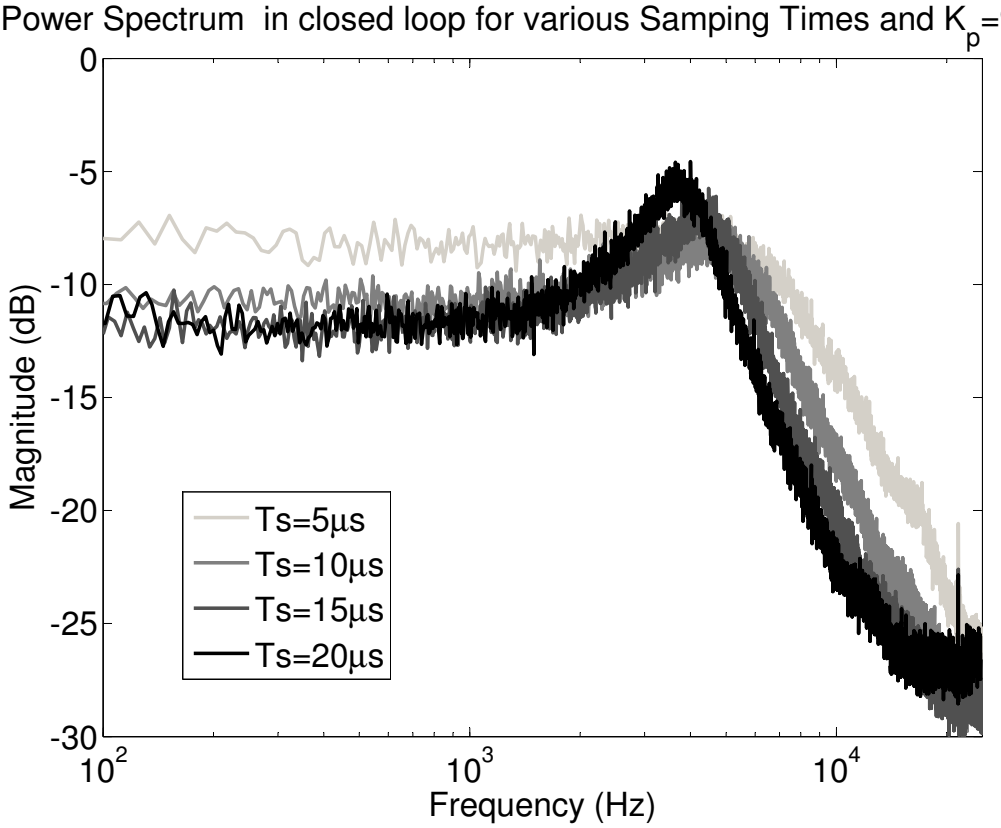

Figure 4.6: The figure shows thermal noise power spectrum of the photodetector output for different values of feedback loop delay. Note that the onset of peak in the power spectrum occurs at lower frequency as the sampling time, T_s, is increased.

4.3.4 Frequency sweep based system identification

It is evident from above discussion that the physical modeling that is widely used in the optical tweezers literature does not suffice to account for high frequency behavior in the closed loop setting. We apply the frequency sweep input based plant identification method to the optical tweezers system, which is particularly important for plant identification when delay elements are present, eg. the actuator (AOD in our case) and loop delay of controller. The block diagram for this scheme is shown in Figure 4.7(a), where the external force, F_e, is applied to the trapped bead by introducing an input, d, as shown in Figure 4.7(a).

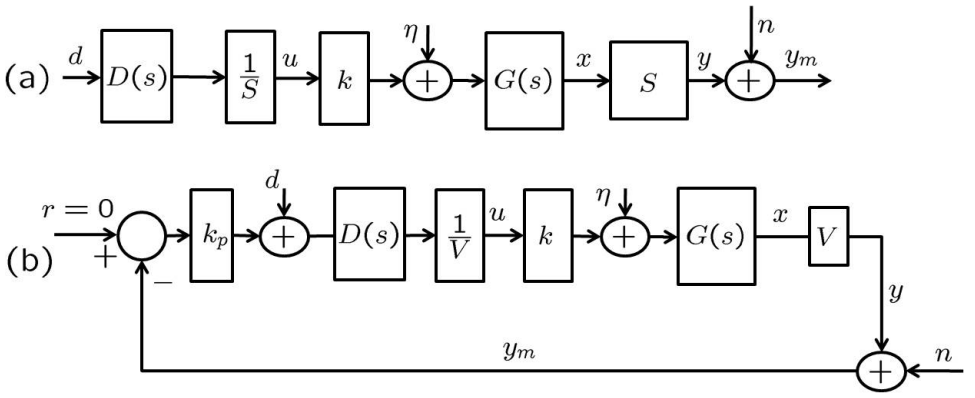

Figure 4.7: (a) Block diagram of our optical tweezers experimental setup. Thermal noise force, η, is the input to the plant and the input d is applied as controller input rather than directly at the plant. (b) Block diagram of our experimental setup in the closed loop. r is the reference signal that is maintained at zero, k_p is the proportional gain of the feedback and $D(s)$ captures the transfer function of the controller and actuator delays. The input d is again applied as a controller input.

A frequency chirp input is applied as the controller input, d, and the output y_m measured. The amplitude of chirp is chosen to reflect the maximum magnitude of the force that might be felt by the bead due to the external force under study, eg. the force the bead may experience due to locomotion of a motor protein. The input, d, and output, y_m give the transfer function $H(s) = kD(s)G(s)$. Figure 4.8 shows the experimentally obtained bode plot for $H(s)$, along with a the transfer function fit. The transfer function was estimated using the *tfestimate* and *invfreqs* command in MATLAB by choosing a two zero and two pole model.

Figure 4.7(b), shows the closed loop block diagram of our experimental setup. Unlike Figure 4.4(b), note that the input, d, in our setup is applied as an input to the controller with $H_{CL}(s)$ being the closed loop transfer function between d and y_m.

For $H(s)$ identification, the controller input was given a frequency sweep from 1 Hz to 10 kHz and with an amplitude of 100 nm of trap movement. The FPGA was run at a loop delay of 100 kHz. From the transfer function fit,

$$H(s) = \frac{0.009s^2 - 2282s + 1.465 \times 10^8}{s^2 + 5.997 \times 10^4 + 1.731 \times 10^8},$$

with two complex right half plane zeros.

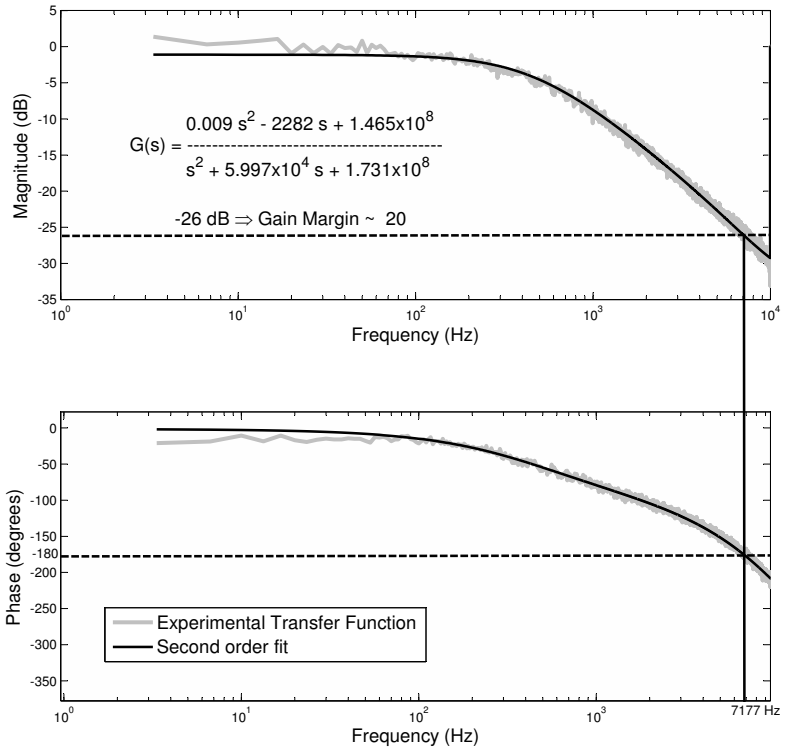

Figure 4.8: The figure shows the Bode plot of experimentally obtained transfer function between the input, d, and measured output, y_m, and its second order fit. This was obtained for a trapped bead of 2.1 μm in diameter. The input to the controller was a frequency sweep from 1 Hz to 10 kHz with the FPGA loop delay set at 10 μs.

Figure 4.9 compares the experimentally obtained power spectrum of the trapped bead for different values of proportional gain in the constant position feedback setting (Figure 4.7 (b)), k_p, with the simulated plots using identified plant, $H(s)$. The identified plant $H(s)$ accounts for all the delays present and explains the peak in the power spectrum. For the proportional gain, $k_p = 13$, in Figure 4.9, note that the experimentally obtained peak is steeper and higher than the simulated peak. This happens because, as the controller gain is cranked up, the control effort increases thereby modulating the trap position in the non linear region.

Figure 4.10 compares the experimentally obtained square wave response to the open loop system as shown in Figure 4.7 (a) with the simulated response using identified transfer function $H(s)$. The frequency of square wave input in Figure 4.10(a) and (b)

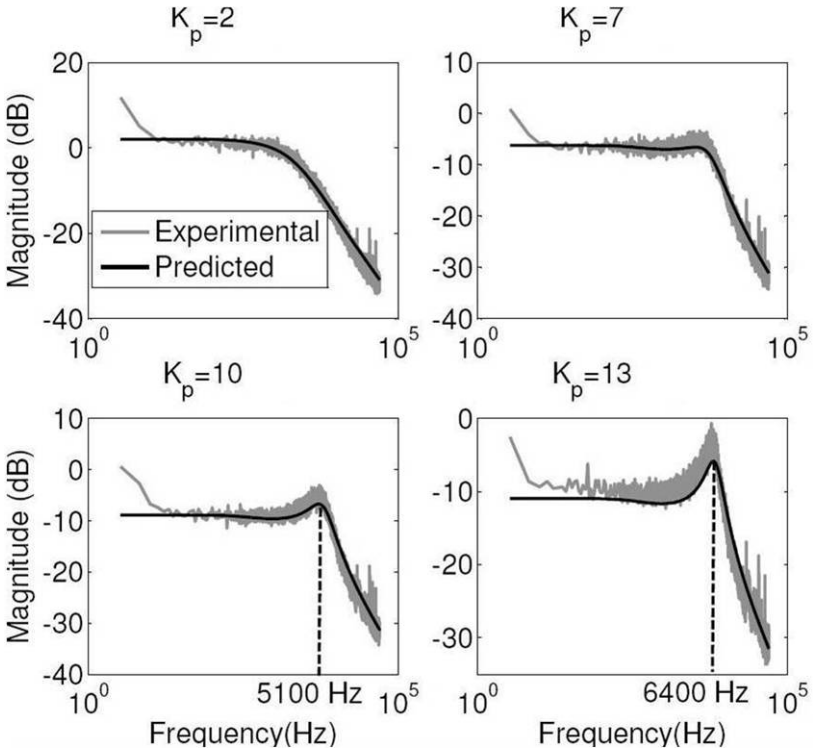

Figure 4.9: The figure compares the experimentally obtained power spectrum for a 2.1 μm dia. bead with analytical spectrum predicted from identified plant, $H(s)$, for various values of proportional gain, k_p.

was 100 Hz and 600 Hz respectively. From Figure 4.10(b) it can be seen that the output, y_m, of the plant no longer resembles the square input, $d(t)$.

4.3.5 Gain Margin

From the bode plot of $H(s)$, in Figure 4.8, gain margin is found to be 26 dB, that corresponds to maximum proportional gain, k_p of 20 for the system to remain stable. This puts a theoretical limit on the maximum gain, however this limit is never reached because of the non-linearities. In Figure 4.5, as k_p is increased the frequency at which peak occurs in power spectrum increases and approaches the theoretical limit of 7.2 kHz, which is the frequency at which phase crosses -180 $degrees$.

The transfer function, $H(s)$, estimated by this method also contains quantitative

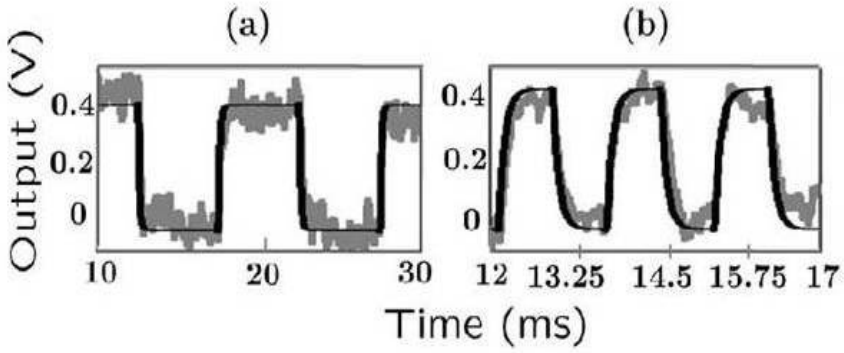

Figure 4.10: The figure shows the experimental and simulated output, obtained when the input, d, is a 80 nm square input in the open loop setting. The frequency of square wave is 100 Hz, and 600 Hz (a) and (b). The experimentally obtained y_m is shown in gray and the simulated output using the identified transfer function, $H(s)$, is shown in black.

information about the delays in the system. To compute that, consider the open loop transfer function, $G(s)$, obtained from the conventional power spectrum method [40],

$$G(s) = \frac{k}{\beta s + k}.$$

At the phase crossover frequency of $H(s)$, i.e. 7.2 kHz, phase of $G(s)$ is $tan^{-1}(2\pi\beta \times 7200/k = 1.57\ rad.$ $H(s)$ has a phase of $-2\pi\ rad$ at this frequency. If we attribute this extra phase contribution to the delays in the system, we get

$$2\pi f_s T_d = 2\pi - 1.57,$$
$$T_d \approx 35\mu s.$$

4.4 Limitations imposed by RHP Zeros

The presence of RHP zeros in the loop transfer function, $L(s) = H(s)D(s)$, for any stabilizing controller $D(s)$ impose restrictions on the achievable performance. The plant transfer function, $H(s)$, identified using the frequency sweep based method has one real or two complex conjugate right half plane zeros (depending on the order of transfer function used to fit the experimentally obtained transfer function). The weighted sensitivity integral (also called the second waterbed formula) states that for a loop transfer

function, $L(s)$, having a single real RHP zero z or a complex conjugate pair of zeros $z = x \pm jy$, and has N_p RHP poles, p_i, then for closed loop stability, the sensitivity transfer function, $S(j\omega) = (1 + L(j\omega))^{-1}$, must satisfy

$$\int_0^\infty ln|S(j\omega)|\mathcal{W}(z,\omega)d\omega = \pi \prod_{i=1}^{N_p} \left| \frac{p_i + z}{p_i - z} \right|, \tag{4.5}$$

where if the zero is real

$$\mathcal{W}(z,\omega) = \frac{2z}{z^2 + \omega^2} = \frac{2}{z} \frac{1}{1 + (\omega/z)^2}, \tag{4.6}$$

and if the zero pair is complex ($z = x \pm jy$)

$$\mathcal{W}(z,\omega) = \frac{x}{x^2 + (y - \omega)^2} + \frac{x}{x^2 + (y + \omega)^2}. \tag{4.7}$$

The identified plant, $H(s)$, has no unstable pole (and under the assumption that $D(s)$ is also stable), therefore

$$\int_0^\infty ln|S(j\omega)|\mathcal{W}(z,\omega)d\omega = 0. \tag{4.8}$$

The weighting function, $\mathcal{W}(z,\omega)$, effectively cuts off the contribution from $ln|S|$ to the weighted sensitivity integral at frequencies $\omega > z$. The weight $\mathcal{W}(z,\omega)$ can be thought of as a first order low pass filter with a cut off frequency at z. Also, $|S|$ is very close to unity at high frequencies (as the complimentary sensitivity function, $(T(s) = 1 - S(s))$, is close to zero at high frequencies to filter out the high frequency measurement noise). Therefore the infinite weighted sensitivity integral can be approximated by a finite sensitivity integral, given by

$$\int_0^z ln|S(j\omega)|d\omega \approx 0. \tag{4.9}$$

This is finite waterbed and imposes a limit on the achievable bandwidth on position regulation, i.e. frequency range,

$$[0, \omega_c] = \{\omega : |S(j\omega)| < m_p, \text{ where } m_p < 1 \text{ is the desired performance objective}\}.$$

The above qualitatively explains that to satisfy the finite waterbed effect, as m_p is reduced further or as ω_c is increased, an increase in the magnitude of $S(j\omega)$ is unavoidable in the region where $|S(j\omega)| \geq 1$ ($\forall\ \omega \leq z$).

Chapter 5

High Bandwidth Force Estimation: Classical Approach

The previous chapter described characterization of the optical tweezers plant by various methods. In this chapter we propose a classical control based strategy that uses the model developed in chapter 4 in the investigation of external forces acting on the trapped bead by using the trapped bead as a probe. The methodology described here depends on accurate characterization of optical tweezers plant, that relies heavily on identifying all components of optical tweezer system, including system latencies.

Feedback control further enhances the efficacy of optical tweezers in sensitive experiments. There are two feedback implementations, viz. position feedback [12] (isometric clamp) where the trap position is regulated to maintain a desired position of the trapped bead, and the force feedback [20] (isotonic clamp) where the force on the trapped bead is regulated by maintaining desired displacement between the trap and the bead. These feedback schemes are used in in-vitro studies of motor protein dynamics (kinesin [46], myosin [12]) and understanding the processes involving nucleic acids [32, 7] (stall forces in RNA, DNA transcription and translation). However, these assays require slow process dynamics [12] (time constants in tens of milliseconds) to estimate the discrete steps of motor movements, which is achieved by maintaining low ATP concentration in the buffer [12, 47] and limiting the number of adsorbed motor molecules [12] on the bead being used as a handle. At higher concentrations, motor movement along microtubule

appears continuous, thereby losing information about fast dynamics. In this chapter we present a new perspective to overcome the challenges involved in the investigation of faster dynamics that require force estimation at high bandwidth for constant position optical tweezers.

Often the position of the bead is measured using a photodiode [12] that collects the laser that has passed through the bead. For the photodiode measurement to remain effective, the bead displacement has to be smaller than a few hundreds of nanometers [55]. Thus feedback strategies become important, wherein based on the bead position measurement, a reference position close to zero is regulated to maintain measurement viability [55]. Also, the regulating force, F_r, (refer Figure 5.1) applied on the bead becomes a measure of external forces acting on the bead.

In this Chapter, it is shown that the regulating force does not provide an effective measure of the external force, if the external force being exerted has high frequency content. The main contribution of this chapter is a methodology, which overcomes limitations of using the regulating force as a measure of external forces, that is based on model identification introduced in Section 4.3.4. To this end, an estimation scheme to estimate the input force is proposed in Section 5.1, which is based on plant inversion followed by Wiener filtering that leads to higher temporal resolution. The experimental results obtained using system inversion scheme are presented in Section 5.2 and these results are compared with those obtained using conventionally used approach of force estimation.

5.1 Inversion based estimation

The dynamics of an optical tweezers system, whilst in the linear region, can be represented by a first order spring damper system with a damping coefficient, β. Position regulation in an isometric clamp increases the effective trap stiffness thereby reducing the Brownian excursions of the trapped bead. Position feedback offers force rejection and drift cancellation that helps maintain the trapped bead within linear region of photodiode sensing.

Increased stiffness due to position regulation does reduce Brownian motion of the trapped bead. However, it also leads to the decreased sensitivity of the trapped bead

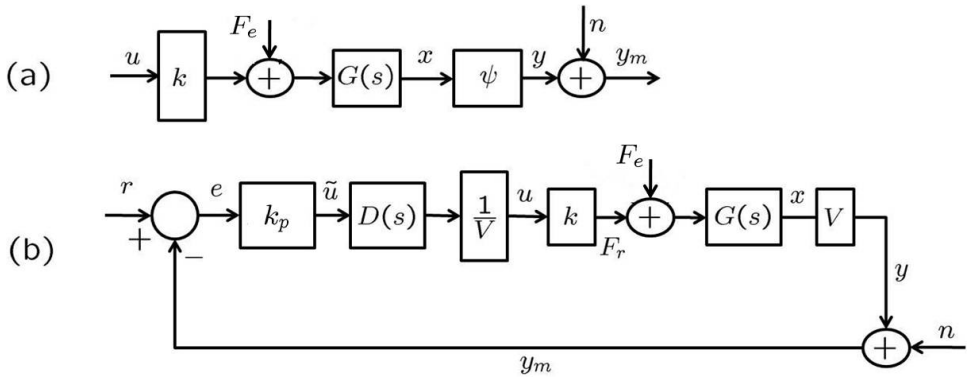

Figure 5.1: The figure shows the block diagram of optical tweezers system in (a) with η, F_e and u as inputs to the plant $G(s)$. x is the bead position, ψ is the map that provides the photodiode voltage for a given bead position and is nonlinear, n is measurement noise and y_m is photodiode output. (b) shows the block diagram of constant position optical tweezers with reference, r, kept at 0. V is the constant photodiode sensitivity in the linear region of operation. In both these figures, the external force, F_e, is assumed to depict the thermal noise force and any other force experienced by the trapped bead.

to the forces on the bead that need to be estimated as these forces affect the bead dynamics exactly the same manner in which the Langevin force effects the dynamics. The control input, i.e. actuator output, is a reflection of the forces sensed by the trapped bead. However, the control input (as explained later) provides a good estimation of forces for low bandwidth operation and fails at high bandwidth. This limitation is not circumvented even at higher values of proportional gain as it leads to operating optical tweezers beyond the linear region of trap stiffness. The delays involved in the controller and actuator response further impose an upper limit (Sec. 4.3.5) on the feedback gain. Therefore, the regulating force, $F_r = ku$, alone does not provide a good estimate of external force, F_e, exerted by the biomolecule, if F_e has high frequency content.

Figure 5.1 shows the open loop and closed block diagram of optical tweezers plant with a proportional feedback gain, k_p. The external inputs to the system, i.e. the thermal noise force and any other external force are jointly depicted as F_e in Figure 5.1.

In traditional open-loop schemes (Figure 5.1(a)), the scaled photodiode output $F_o = ky_m/V$ is considered as an estimate of the force F_e [48, 49]. In this case

$$F_o(s) = kG(s)F_e(s) = k\frac{1}{\beta s + k}F_e(s), \tag{5.1}$$

where F_o provides a good estimate [48, 49] of F_e if the Fourier transform of F_e is negligible beyond the cut-off frequency, $f_G = k/2\pi\beta$.

In the position clamp feedback setup (Figure 5.1(b)), the measured bead position is compared to a reference position, r, and based on the error, $e = r - y$, the controller provides a regulating force, $F_r = ku$. When a proportional gain controller [53] with gain k_p is chosen, the closed loop transfer function with input F_e and output F_r, in Figure 5.1(b), is given by

$$F_r(s) = \frac{k_p H(s)}{1 + k_p H(s)} F_e(s) \tag{5.2}$$

where $H(s) = kG(s)D(s)$, where $D(s)$ captures latencies in the controller implementation. In existing work it is assumed that the AOD instantly changes the trap position, u, once the command to change the trap position is given. Thus the existing feedback strategies (4.2), fail to capture the latencies (characterized by $D(s)$ in Figure 5.1(b)) and dynamics of components, like the AOD dynamics, that make them unsuitable for high bandwidth operation.

A traditional closed-loop configuration [12] and analysis results from Figure 5.1(b) if $D(s)$ is set to 1, where $F_{ra} = ku$ is considered as an estimate of the external force F_e. The closed-loop transfer function that relates F_e to F_{ra} (with $D(s)$ set to 1) is given by

$$F_{ra}(s) = \frac{\tilde{H}(s)}{1 + \tilde{H}(s)} F_e(s), \tag{5.3}$$

where $\tilde{H}(s) = kG(s)k_p$. Thus substituting for $G(s)$ we have

$$F_{ra}(s) = \frac{kk_p}{\beta s + k(1 + k_p)} F_e(s). \tag{5.4}$$

The assumption that latencies represented by $D(s)$ can be ignored [48] is reasonable if the external force F_e is such that $F_e(s)$ is negligible beyond the cut-off frequency f_D of the filter $D(j\omega)$. In such a case, F_{ra} (see (5.4)) is a good approximation [48] of F_r (see (5.2)) and Fourier components of F_e are accurately reconstructed up to the cut-off frequency, $f_{cla} = \frac{k(1+k_p)}{2\pi\beta}$ (see (5.4)). It is to be noted that the assumed closed-loop cut-off frequency is $f_{cla} = f_G + \frac{kk_p}{2\pi\beta}$. Thus the closed-loop strategy increases the frequency up to which F_e can be correctly estimated increases by $\frac{kk_p}{2\pi\beta}$ over the open loop estimate. This advantage is limited as the controller gain k_p has to be small enough to maintain stability [55] of the closed-loop and has to satisfy $f_{cla} < f_D$.

In the open loop case (Figure 5.1(a)), the plant transfer function, $G(s) = 1/(\beta s+k)$, can be determined by using the traditional power spectrum method given in Section 4.3.1. For the closed loop block diagram (Figure 5.1(b)), the transfer function $D(s)$ characterizing system latencies can be obtained from $H(s) = kD(s)G(s)$, which can be obtained using the frequency sweep method explained in Section 4.3.4. This limitation in estimating the external force, F_e, beyond the cut-off frequencies f_G and f_{cla} in open loop and closed loop implementation, respectively, can be significantly alleviated by employing the *classical controls* method of system inversion.

The model obtained can be inverted to estimate the external force, F_e, over a larger frequency range. In the open loop case, F_e passes through the filter $G(j\omega)$ to yield the output $x = y/V$ that is corrupted by noise. Thus to obtain an estimate of F_e, $y_m/V = (y+n)/S$ (where n is the measurement noise) can be filtered using the filter $G^{-1}(j\omega) = j\beta\omega + k$. Thus, open-loop estimate is provided by $G^{-1}(j\omega)(Y(j\omega) + N(j\omega))/V)$. As $G^{-1}(s)$ is a high pass filter, it will unacceptably enhance the effect of noise and thus a better estimate can be obtained by introducing a stable low pass transfer function $Q(s)$ of the form $\frac{2\pi f_Q}{s+2\pi f_Q}$, where f_Q is the cut off frequency of Q, which is chosen depending on the strength of the measurement noise. The signal y_m is filtered by $Q(j\omega)G^{-1}(j\omega)$ to yield the estimate

$$\tilde{F}_o(j\omega) = Q(j\omega)F_e(j\omega) + Q(j\omega)G^{-1}(j\omega)N(j\omega)/V \tag{5.5}$$

that provides a good estimate of F_e up to the cutoff frequency, f_Q.

A similar method when employed for closed-loop operation of the system is more challenging. The transfer function that relates F_e to F_r (see Figure 5.1(b)) as presented earlier is $\frac{k_pH(s)}{1+k_pH(s)}$ that has right half plane zeros due to the transfer function $D(s)$ characterizing latencies in the system. The inverse filter required to estimate the external force, F_e, from F_r will be of the form $\frac{1+k_pH(s)}{k_pH(s)}$. This inverse filter is unstable as it involves factors right half plane poles. This challenge can be overcome by performing a minimum phase inversion of the transfer function $\frac{k_pH(s)}{1+k_pH(s)}$, where the right half plane zeros are replaced with their minimum phase counterparts. A closer look at the closed loop block diagram, however, provides another readily available closed-loop signal y_m that circumvents this problem. The closed-loop filter that relates F_e to y_m/V is $G(s)/(1 + k_pH(s))$ that has a stable inverse and can be implemented. Like in the

open loop case, a low pass filter $Q(s)$ is used to mitigate the measurement noise. Thus a closed-loop estimate, $\tilde{F}_{cl}$, can be obtained by using the filter $\frac{Q(s)(1+k_pH(s))}{G(s)}$ on y_m/V as provided below

$$\tilde{F}_{cl}(s) = Q(s)F_e(s) + \frac{Q(s)}{G(s)}\frac{N(s)}{V}, \tag{5.6}$$

that yields a good estimate of F_e up to the cutoff frequency of the filter $Q(s)$.

The estimate of external force input, F_e, thus obtained contains the effect of thermal noise that can be reduced by treating the estimates $\tilde{F}_o$ and $\tilde{F}_{cl}$ by appropriately designed Wiener filter, given by

$$\mathcal{F}^{-1}\left(\underbrace{\frac{S_{vv}(\omega)}{S_{vv}(\omega)+S_{\eta\eta}(\omega)}}_{WienerFilter}V(\omega)\right), \quad \left\{v = \begin{array}{ll} \tilde{F}_o, & \text{open loop case} \\ \tilde{F}_{cl}, & \text{closed loop case} \end{array}\right\} \tag{5.7}$$

where $\mathcal{F}^{-1}$ is the inverse Fourier transform, $S_{vv}(\omega)$ and $S_{\eta\eta}(\omega)$ is the Fourier transform of the autocorrelation of $v(t)$ and $\eta(t)$ respectively and $V(\omega)$ is the Fourier transform of $v(t)$. Thermal noise power spectral density, $S_{\eta\eta}(\omega)$, is given by $2k_BT\beta$, where k_B is the Boltzmann constant and T is the absolute temperature. The Wiener filter helps reduce the effect of thermal noise, η, in the estimation of the external force that is to be measured.

5.2 Experimental Results based on System Inversion

Using the method of power spectrum density, k and β were determined to be $k = 0.05$ pN/nm and $\beta = 1.76 \times 10^{-5}$ $pNsec/nm$ and the photodiode sensitivity constant, V, was found to be 5 mV/nm (Sec. 4.2.3). The frequency sweep based method was used to identify the transfer function $H(s) = kD(s)G(s)$ by providing a constant amplitude chirp input having a frequency range of 1 to 20 kHz. From the experimentally obtained data the transfer function of $H(s)$ was estimated by doing a transfer function fit (see Figure)using *MATLAB* by choosing a 2 zeros and 3 poles model. The transfer function was found to be

$$H(s) = \frac{992.5s^2 - 2.05e8s + 1.6e13}{s^3 + 8.5e3s^2 + 3.8e9s + 1.06e13}, \tag{5.8}$$

having right half plane zeros at $z_1 = 110$ $krad/s$ and $z_2 = 97$ $krad/s$.

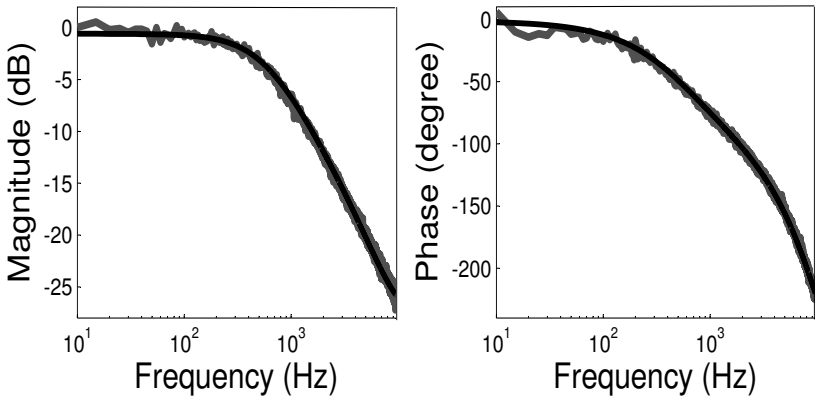

Figure 5.2: Shows the frequency response of transfer function, $H(s)$, obtained experimentally (in gray) and its estimate (in black).

The estimates of input force F_e obtained using the traditional methods and the method of system inversion proposed in Section 5.1 for both open loop and closed loop case are shown in Figure 5.3 and Figure 5.4. The limitations on the bandwidth of force estimation in both open-loop and closed-loop cases using the traditional approach is evident in Figure 5.3 and Figure 5.4 respectively, which shows experimental data comparing F_e (black solid curve) and the traditional estimates when F_e has high frequency content. F_e is a periodic wave of 1 kHz in Figure 5.3(a) and Figure 5.4(a) and 5 kHz in Figure Figure 5.3(b) and Figure 5.4(b). Figure 5.3(a) and 5.3(b) show the open-loop estimates F_o (gray broken curve) and Figure 5.4(a) and 5.4(b) show the traditional closed-loop estimates F_{ra} (gray broken curve). It is evident that traditional estimates [48, 49], F_o and F_{ra} are not a good measure of the high bandwidth, more rapidly changing force profile.

Figure 5.3(a) and 5.3(b) also show the open-loop estimate, $\tilde{F}_o$, as obtained by the method developed in the paper (gray solid curve), where the 1 kHz and 5 kHz periodic force F_e is accurately predicted. The external force, F_e, experienced at the trapped bead has an amplitude of 5 pN (except in the region, where overshoots and undershoots are seen). It was confirmed that the force estimate obtained using the traditional method failed for a similar periodic profile of external force F_e at even 500 Hz (plot not shown).The experimental data confirms that using the method of system inversion, the temporal resolution of the external force estimation is improved by an order of

magnitude in the open-loop case.

Figure 5.4(a) and 5.4(b) show the closed loop estimate $\tilde{F}_{cl}$ (gray solid line) obtained using (5.6) where the 1 kHz and 5 kHz periodic force F_e is accurately predicted. The input force, F_e, was generated by applying a square wave input, d, with 500 mV amplitude at 1 kHz and 5 kHz. The cut off frequency, f_Q, for the filter Q was chosen to be 100 kHz and k_p was set to 2. Figure 5.4(a) and 5.4(b) illustrate that the system inversion method is capable of estimating the periodic square wave like force profile with a frequency of 5 kHz whereas the traditional estimate fails at 1 kHz. The square wave like periodic force has a significant contribution from second and third harmonics (which appear respectively at 3 and 5 times of the fundamental frequency), which implies that in the closed loop case also, an order of magnitude increase in temporal resolution of force estimation is achieved by the system inversion method.

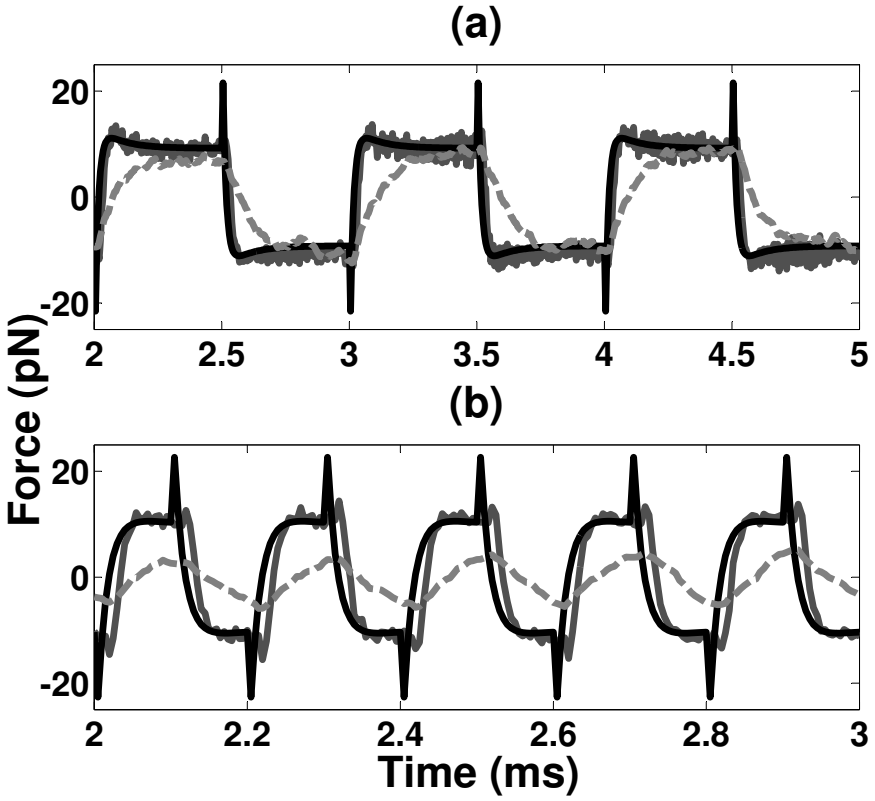

Figure 5.3: Shows a comparison between the input force, F_e (black solid line), the estimate of input force by the method of system inversion and the force estimate obtained using traditional methods for the open loop case. A periodic force, F_e, with a frequency of 1 kHz and 5 kHz in (a) and (b) respectively, is compared with $\tilde{F}_o$ (gray solid line) and F_o (gray broken line). The effect of thermal noise, η, was reduced from estimates by applying a Wiener filter.

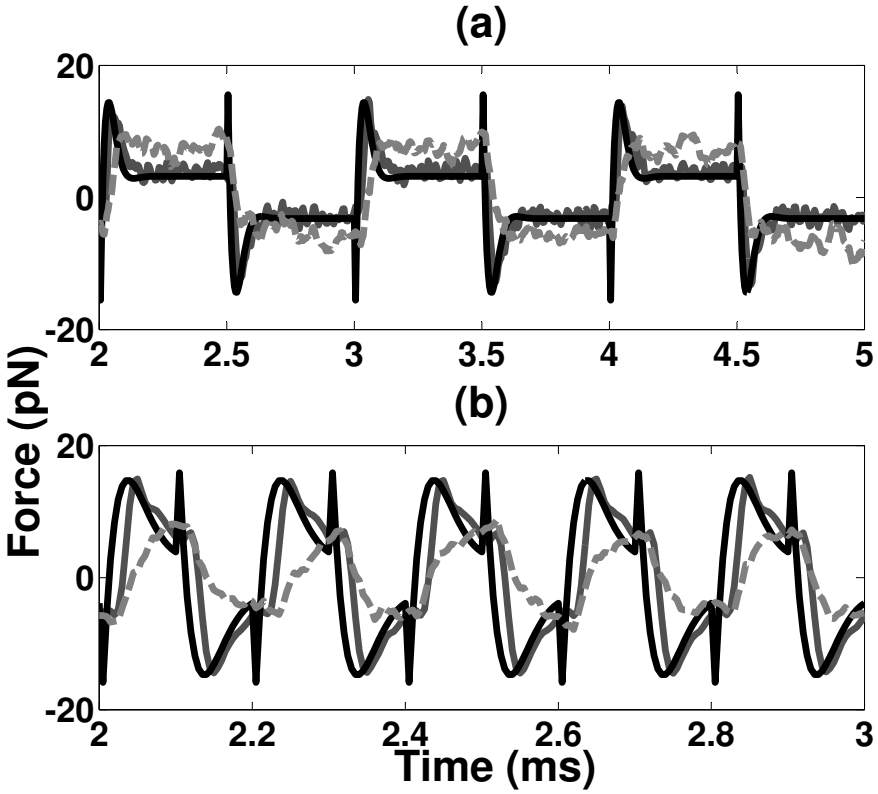

Figure 5.4: Shows a comparison between the input force, F_e (black solid line), the estimate of input force by the method of system inversion and the force estimate obtained using traditional methods for the closed loop case. A periodic force, F_e, with a frequency of 1 kHz and 5 kHz in (a) and (b) respectively, is compared with $\tilde{F}_{cl}$ (gray solid line) and F_{ra} (gray broken line). The effect of thermal noise, η, was reduced from estimates by applying a Wiener filter.

Chapter 6

High Bandwidth Force Estimation: Modern Controls Approach

The previous chapter discussed the need of high bandwidth force estimation for biomolecular assays at native concentrations and the limitation of estimating the external force experienced by a trapped bead using the traditional methods was highlighted. The approach of system inversion by inverting the well characterized optical tweezers plant was presented in Chapter 5 that enabled estimation of fast force dynamics experienced by the trapped bead. It was shown experimentally that more than an order of magnitude increase in the bandwidth of external force estimation was achieved using the method of system inversion. However, the scheme presented in Chapter 5 for estimating the external force, F_e, is qualified by the structure imposed on the control strategy, i.e. proportional only or proportional-integral controller, followed by an ad-hoc inversion of the map from F_e to measured output, y_m, which results in a below-optimal performance.

This chapter proposes a scheme to overcome the inadequacy of system inversion approach by searching for the optimal control strategy over the space of all stabilizing linear controllers. An introduction to the definitions and robust control preliminaries is presented in Section 6.1 that form the basis of discussion in further sections. In Section 6.2, the problem of using constant position optical tweezer as a force probe for

measuring external force having high frequency content is casted in a robust control framework, where constant position regulation of the trapped bead and estimation of external force are set as specific performance objectives. In this optimal framework, it is demonstrated, in Section 6.3, using simulation and with experimental results that the bandwidth of force estimation is further improved over the system inversion strategy.

6.1 Definitions and Robust Control Preliminaries

This section discusses the mathematical definitions and control framework that forms the basis of the robust control approach developed in Section 6.2.

Consider a closed loop block diagram of a system $G(s)$ in a negative feedback configuration with a controller $K(s)$ as shown in Figure 6.1. The desired reference signal is denoted by r, the input to plant is denoted by u which is the output of controller, $K(s)$, the disturbance to the plant at its output is denoted by d, the output signal is y and y_m is the measured output which is a corrupted version of y by addition of measurement noise, n.

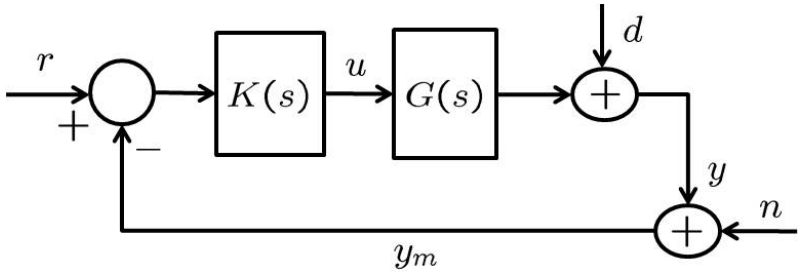

Figure 6.1: Block diagram of a plant, $G(s)$, with input $u(t)$. A disturbance signal $d(t)$ gets added at the output stage resulting in an output $y(t)$. The measurement noise is denoted by $n(t)$ and $y_m(t)$ is the measured output. The measurement $y_m(t)$ is compared with a desired reference signal $r(t)$ in a negative feedback configuration with $K(s)$ as the transfer function of controller.

The output, y, in terms of inputs to the closed loop system (r, d and n) can be written as

$$y(s) = \frac{G(s)K(s)}{1+G(s)K(s)}r(s) + \frac{1}{1+G(s)K(s)}d(s) - \frac{G(s)K(s)}{1+G(s)K(s)}n(s), \quad (6.1)$$

$$y(s) = T(s)r(s) + S(s)d(s) - T(s)n(s). \quad (6.2)$$

The tracking error, denoted by $e(t) = r(t) - y(t)$, can be written in terms of inputs to closed loop system as

$$e(s) = S(s)r(s) - S(s)d(s) + T(s)n(s). \tag{6.3}$$

where the closed loop transfer functions $S(s) = \frac{1}{1+G(s)K(s)}$ and $T(s) = \frac{G(s)K(s)}{1+G(s)K(s)}$ are the sensitivity transfer function and complementary sensitivity transfer function, respectively, and satisfy the constraint $S(s) + T(s) = 1$.

The typical performance objectives in a closed loop setup as shown in Figure 6.1 are reference tracking, *i.e.* output y tracks reference r, disturbance rejection, *i.e.* the effect of disturbance signal, d, on output y is minimized and good resolution, *i.e.* the output y is small when the only input to system is measurement noise, n. From 6.3 is it seen that for good reference tracking, the magnitude of transfer function from reference input, r, to tracking error , e, given by $S(s)$ needs to be small in the frequency range that contains that contains the reference signal r. Similarly it can be argued from (6.2) that for good disturbance rejection, the magnitude of transfer function from d to y given by $S(s)$ needs to be small in the frequency range containing frequency content of d and for good resolution the magnitude of transfer function from measurement noise, n, to output, y, given by $T(s)$ be small. These performance objectives can be simultaneously met irrespective of the constraint on sensitivity and complementary sensitivity transfer functions ($S(j\omega) + T(j\omega) = 1$) by designing $S(j\omega)$ and $T(j\omega)$ such that the magnitude of $S(j\omega)$ is small in the low frequency region as the reference signal and disturbance to the plant are typically low frequency signals and magnitude of $T(j\omega)$ is kept low in the high frequency region as noise, n, is a high frequency phenomenon.

The design of $S(s)$ and $T(s)$ is called closed loop shaping and is achieved by carefully designing weighting functions $W_s(s)$ and $W_t(s)$, such that

$$S(j\omega) \leq W_s(j\omega) \text{ and } T(j\omega) \leq W_t(j\omega), \forall\ \omega. \tag{6.4}$$

In terms of the H_∞ norm of a transfer function, (6.4) can be rewritten as

$$\|W_s S\|_{H_\infty} \leq 1 \text{ and } \|W_t T\|_{H_\infty} \leq 1, \tag{6.5}$$

where the H_∞ norm of a function $f(s)$ is defined as

$$\|f\|_{H_\infty} = sup_\omega |f(j\omega)|.$$

The selection of weighting functions $W_s(s)$ and $W_t(s)$ is an engineering problem involving design of these transfer functions such that magnitude of closed loop transfer functions $S(s)$ and $T(s)$ remains lower than the magnitude of $1/W_s(s)$ and $1/W_t(s)$ in the desired frequency range. There exists a complete theory of controller synthesis where a controller transfer function $K(s)$ is searched over the space of all stabilizing linear controllers such that the condition given by 6.5 is satisfied. Typically, the controller $K(s)$ is obtained using the H_∞ solver in *MATLAB* software which solves the stacked constraint problem

$$arg \quad \underset{K \text{ stabilizing}}{min} \left\| \begin{array}{c} W_s S \\ W_t T \end{array} \right\|_{H_\infty} .$$

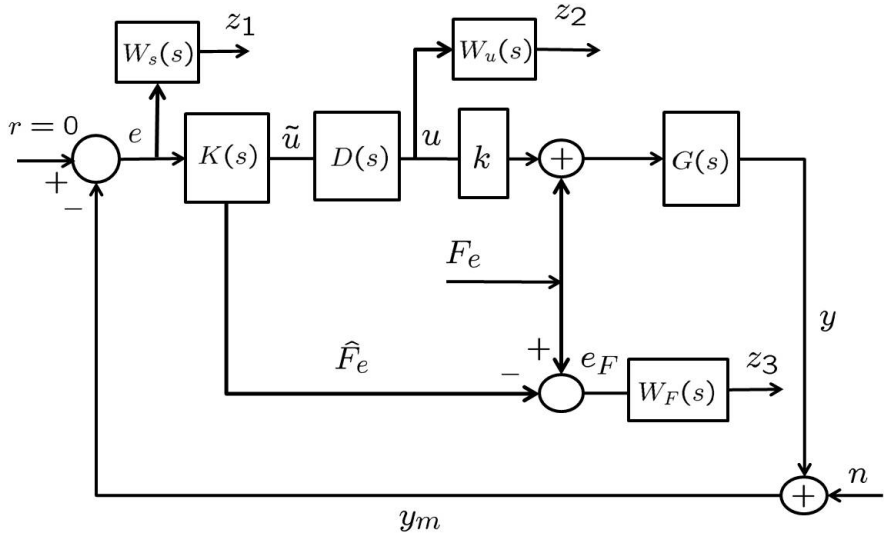

Figure 6.2: Block diagram of the constant position optical tweezers system in the robust control framework. The inputs to the system are the reference signal, r, that is maintained at a constant position (say 0), the external force input, F_e, which includes both the thermal noise force, η, and any other external force and the measurement noise, n. k is the trap stiffness, u is the control input, y is the instantaneous position of the bead (in Volts), y_m is the measured photodiode output and e is the regulation error given by $r - y_m$. The transfer functions $G(s)$, $K(s)$ and $D(s)$ represent the optically trapped bead, the controller and the transfer function capturing the system latencies, respectively. The estimate of external force input, F_e, is denoted by $\hat{F}_e$ and the error in estimation is denoted by e_F. The weighting functions for the performance objectives of constant position regulation, bounded control input and estimation of F_e are given by $W_s(s)$, $W_u(s)$ and $W_F(s)$, respectively, with z_1, z_2 and z_3 being the corresponding regulated variables.

6.2 H-infinity based estimation

In this section the performance objectives for constant position regulation of optical tweezers are identified and an optimal strategy is developed that results in further increase in the bandwidth of external force estimation over the system inversion method in Section 5.1. It should be noted that the primary objective of constant position optical tweezers is finding an estimate, $\hat{F}_e$ of external force, F_e. The other performance objectives are constant position regulation and maintaining the validity of linear spring assumption of an optical trap by keeping the control input, u, within certain limits. The problem of satisfying these performance objectives is casted in a robust control framework (refer Section 6.1), where an optimal strategy is developed by simultaneously optimizing for identified performance objectives. To this end, an optimal control strategy is formulated where the objectives of constant position regulation, bounded control input and estimation of external force input are captured by regulated variables $z_1 = W_s e$, $z_2 = W_u u$ and $z_3 = W_F e_F$ as shown in Figure 6.2. The regulated variables z_1, z_2 and z_3 are weighted regulation error, weighted control effort and weighted estimation error respectively. The optimal control problem is to synthesize a two by one transfer function $K(s) = [K_1(s)\ K_2(s)]^T$ such that the H-infinity norm of the transfer function map from external inputs r, n and F_e to regulated variables z_1, z_2 and z_3 is minimized. Mathematically this can be written as

$$K(s) = [K_1(s)K_2(s)]^T = arg \min_{K(s)=[K_1(s)\ K_2(s)]^T stabilizing} \|M(s)\|_{H_\infty}, \tag{6.6}$$

where $M(s)$ is such that $[z_1\ z_2\ z_3]^T = M(s)[r - n\ F_e]^T$. The controller transfer function $K_1(s)$ alone decides the performance objectives of constant position regulation and bounded control input, while the transfer function $K_2(s)$ decides the estimation error, e_F in conjunction with $K_1(s)$. The estimation error, e_F, is defined to be $F_e - \hat{F}_e$ and is required to be low for a big enough bandwidth for good estimation of the external force input, F_e. It is to be noted that the block schematic of optimal control strategy shown in Figure 6.2 is obtained from the closed loop block diagram shown in Figure 4.4(b), where the blocks representing the linear sensitivity constant given by V and $1/V$ have been omitted for simplicity and the external inputs $\eta + F_e$ are both clubbed into F_e. Therefore $\hat{F}_e$ in Figure 6.2 depicts estimate of $\eta + F_e$. The estimate $\hat{F}_e$ can

be treated with an appropriately designed Wiener Filter to get an estimate of only the external force input. As explained in Section 6.1, to meet the performance objectives, it is desired to have the magnitude of map (transfer function) from reference signal, r, to regulation error, e; from external inputs to control effort u and from external input force F_e to estimation error e_F to be small in the desired frequency range. This is achieved by appropriately designing weighting functions described in Section 6.3. Define the *Sensitivity* transfer function, S, and *Complementary Sensitivity* transfer function, T, as

$$S(s) = \frac{1}{1 + kK_1(s)D(s)G(s)} \text{ and} \tag{6.7}$$

$$T(s) = \frac{kK_1(s)D(s)G(s)}{1 + kK_1(s)D(s)G(s)}. \tag{6.8}$$

From Figure 6.2 the regulated variables, z_1, z_2 and z_3, can be written in terms of $S(s)$, $T(s)$ and external inputs r, n and F_e as

$$\begin{bmatrix} z_1 \\ z_2 \\ z_3 \end{bmatrix} = \underbrace{\begin{bmatrix} W_sS & -W_sGS \\ W_uK_1DS & -W_uGK_1DS \\ -W_FK_2S & W_F(1 + K_2GS) \end{bmatrix}}_{M(s)=\mathcal{F}_l(P,K)} \begin{bmatrix} r - n \\ F_e \end{bmatrix}, \tag{6.9}$$

where $\mathcal{F}_l(P, K)$ is the lower fractional transformation for the generalized plant, $P(s)$, with controller $K(s)$. The generalized plant $P(s)$ is given by

$$P = \begin{bmatrix} W_s & -W_sG & -kW_sGD & 0 \\ 0 & 0 & W_uD & 0 \\ 0 & W_F & 0 & -W_F \\ 1 & -G & -kGD & 0 \end{bmatrix}. \tag{6.10}$$

The block diagram for the generalized plant framework is shown in Figure 6.3, where $w = [r - n\ F_e]^T$ is the exogenous input, $z = [z_1\ z_2\ z_3]^T$ is the regulated variable, e is the measured variable and $\tilde{u}$ and $\hat{F}_e$ are the control variables.

The reference position, r, for constant position regulation can be assumed to be 0 without loss of generality, as shown in Figure 6.2. Also the measurement noise, n, can be ignored in (6.9), as its effect can be reduced from the regulated variables by post-filtering. This reduces the optimization problem to finding $K_1(s)$ and $K_2(s)$, such

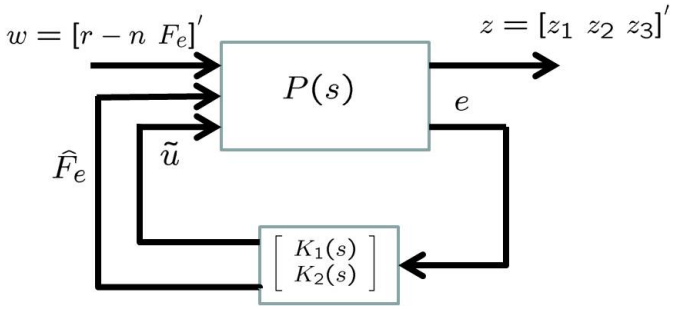

Figure 6.3: The figure shows the generalized plant block diagram with P as the generalized plant, w as the exogenous input, z as the regulated output, e as the controller input and $\tilde{u}$ and F_e as the output of controller $[K_1 \ K_2]'$.

that

$$arg \min_{K=[K_1 \ K_2]^T \ stabilizing} \left| \underbrace{\begin{bmatrix} -W_s GS \\ -W_u GK_1 DS \\ W_F(1 + K_2 GS) \end{bmatrix}}_{\tilde{M}(s)=\mathcal{F}_l(\tilde{P},K)} \right|_{H_\infty}, \tag{6.11}$$

where $\mathcal{F}_l(\tilde{P}, K)$ is the lower fractional transformation for the generalized plant, $\tilde{P}(s)$, with controller $K(s)$. The generalized plant $\tilde{P}(s)$ is given by

$$\tilde{P} = \begin{bmatrix} -W_s G & -kW_s GD & 0 \\ 0 & W_u D & 0 \\ W_F & 0 & -W_F \\ -G & -kGD & 0 \end{bmatrix}. \tag{6.12}$$

The block diagram for the generalized plant framework is shown in Figure 6.4, where $w = F_e$ is the exogenous input, $z = [z_1 \ z_2 \ z_3]^T$ is the regulated variable, e is the measured variable and $\tilde{u}$ and $\hat{F}_e$ are the control variables.

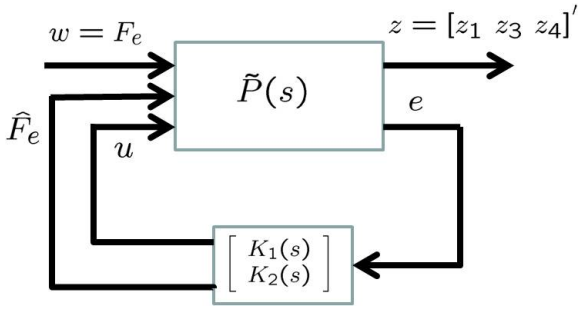

Figure 6.4: The figure shows the generalized plant block diagram with $\tilde{P}$ as the generalized plant, $w = F_e$ as the exogenous input, z as the regulated output, e as the controller input and $\tilde{u}$ and F_e as the output of controller $[K_1\ K_2]'$.

6.3 Experimental Results for H-infinity based estimation scheme

The analytical and experimental results obtained by implementing the control strategy developed in Section 6.2 to meet the performance objectives of position regulation, bounded control input and estimation of high bandwidth external force input is presented in this section. These results are also compared with the results obtained using the method of *System Inversion* presented in Section 5.1 showing the benefits of casting the performance objectives in robust control framework. The optical trap was created a polystyrene bead of diameter 2.1 μm and the transfer function block $G(s) = 1/(\beta s + k)$ in Figure 6.2 capturing the dynamics of optically trapped bead was identified using the method of power spectrum (refer Section 4.3.1). The spring constant k was determined to be 0.02 pN/nm with the drag coefficient β evaluated at room temperature to be $1.76e-5\ Ns/m$. This resulted in a cut off frequency, $f_c = k/2\pi\beta$, for $G(s)$ to be 176 Hz. The transfer function from $\tilde{u}$ to y in Figure 6.2 given by $H(s) = kD(s)G(s)$ was determined using the method of frequency sweep input (refer Section 4.3.4) by doing a 2 zeros and 3 poles transfer function fit to the experimentally obtained transfer function and was found to be $954\frac{s^2-1.61e5s+1.1e10}{(s+1167)(s^2+1.5e5s+9e9)}$. The transfer function block, $D(s)$ in Figure 6.2, capturing the latencies involved in the closed loop system is evaluated to $D(s) = H(s)/kG(s) = 0.86\frac{(s+1111)(s^2-1.61e5s+1.1e10)}{(s+1167)(s^2+1.5e5s+9e9)}$. In Figure 6.2, the constant block, V, denoting the calibration of bead position detection scheme was found to be

5 mV/nm, using the method of photodiode calibration explained in Section 4.2.3. Once, the individual transfer function blocks of Figure 6.2 are accurately characterized, the external force input can be estimated using the method of system inversion [56] and the Robust control method proposed in this paper.

For estimating the external force input, F_e, using the method of system inversion, the choice of proportional and integral gains, given by k_p and k_i respectively, was made by comparing over a large set of values for $\{k_p, k_i\}$ and looking for the set $\{k_p, k_i\}$ that provided the best position regulation for our experimental setup. This was found to be for $k_p = 10$ and $k_i = 10000$. The controller, $K(s) = k_p + k_i/s$, in Figure 4.4(b) and other transfer functions such as sensitivity transfer function, $S(s)$ and complementary sensitivity transfer function, $T(s)$ will be denoted by $K^{PI}(s)$, $S^{PI}(s)$ and $T^{PI}(s)$ for the system inversion case to distinguish from corresponding transfer functions in the robust control framework. Using the system inversion approach, the filter $K_2^{PI}(s)$ is synthesized to be $\frac{1}{G(s)S^{PI}(s)}\frac{2\pi f_Q}{(1+2\pi f_Q)}$, where $G(s)S^{PI}(s)$ is the transfer function from $F_e(s)$ to $y(s)$(note that the constant V has been dropped for simplicity) and the low pass filter $2\pi f_Q/(s+2\pi f_Q)$ is introduced to avoid blowing up the effect of measurement noise as $1/G(s)S^{PI}(s)$ is an improper transfer function.

The goal of synthesizing optimal filters $K_1(s)$ and $K_2(s)$ to meet the three performance objectives listed in Section 6.2 depends on carefully designing the corresponding weighting functions, $W_s(s)$, $W_u(s)$ and $W_F(s)$. These weighting functions were designed, keeping in view the best performance achieved using the system inversion approach, i.e. $K^{PI}(s) = 10+10000/s$. To have the H_∞ norm of each element of the optimization problem in (6.11) less than unity, the weighting functions were selected as $W_s = 1/(GS^{PI})$, $W_u = 1/(GK^{PI}DS^{PI})$ and $W_F = 1/(1 + K_2^{PI}GS^{PI})$ with the added constraint that any right half plane pole appearing in these weighting functions was converted to a left half plane pole thereby keeping the magnitude plot of these transfer functions same. Any pole appearing on the $j\omega$ axis in these weighting functions was replaced by a pole at unity in left half plane. This yielded the weighting functions to be

$$W_s(s) = \frac{56.5s^5 + 9.2e6s^4 + 4.4e11s^3 + 6.9e15s^2 + 1.3e19s + 6.6e21}{s^5 + 2.1s^4 + 1.9e10s^3 + 5.9e14s^2 + 6.6e17s + 6.6e17}, \quad (6.13)$$

$$W_u(s) = \frac{6.6s^4 + 1.1e6s^3 + 5e10s^2 + 7.5e14s + 6.9e17}{s^4 + 2.2e5s^3 + 2.1e10s^2 + 7.1e14s + 6.9e17} \text{ and} \quad (6.14)$$

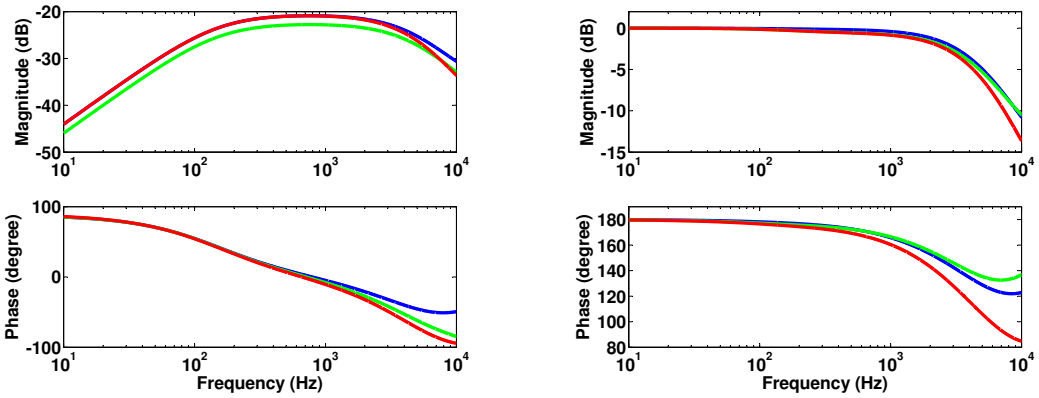

(a) (b)

Figure 6.5: (a) The figure shows the bode plot of the analytical transfer function between F_e and e, given by $G(s)S(s)$, using the robust control framework (green curve) and system inversion process (red curve). The inverse of the weighting function, $W_s(s)$, is shown in blue. (b) The figure shows the bode plot of the analytical transfer function between F_e and u, given by $G(s)K_1(s)D(s)S(s)$, using the robust control framework (green curve) and system inversion process (red curve). The inverse of the weighting function, $W_u(s)$, is shown in blue.

$$W_F(s) = \frac{s + 6.3e5}{s + 1}. \tag{6.15}$$

The optimization problem presented in (6.11) for the weighting functions given in (6.13), (6.14) and (6.15) was solved using the MATLAB solver. The controller $K(s) = [K_1(s)\ K_2(s)]$ was found to be

$$K_1(s) = \frac{5357s^4 + 1.1e9s^3 + 9.1e13s^2 + 2.9e18s + 2.8e21}{s^4 + 2.1e7s^3 + 5e12s^2 + 2.2e17s + 2e17}, \tag{6.16}$$

$$K_2(s) = \frac{1e5s^{14} - 5.6e14s^{13} - 3.4e20s^{12} - 9.6e25s^{11} - 1.6e31s^{10}}{s^{14} + 2.3e10s^{13} + 5.1e17s^{12} + 3.4e23s^{11} + 1e29s^{10}} \frac{-1.8e36s^9 - 1.4e41s^8 - 7e45s^7 - 2.3e50s^6 - 4.5e54s^5 - 4.4e58s^4}{1.8e34s^9 + 2e^39s^8 + 1.5e44s^7 + 7e48s^6 + 2e53s^5} \frac{-1.4e62s^3 - 2e65s^2 - 1.3e68s - 3.4e70}{2.6e57s^4 + 7.4e60s^3 + 7.6e63s^2 + 2.7e66s + 2.4e66} \tag{6.17}$$

The solution ($K_1(s)$ and $K_2(s)$) that minimizes $\|M(s)\|_{H_\infty}$ is optimal among the whole class of linear stabilizing controllers. However, in practice, the MATLAB solver solves this problem for a user-defined $\gamma > \min_K \|M(s)\|_{H_\infty}$ such that $\|M(s)\|_{H_\infty} < \gamma$ and thus the controller $K(s)$ obtained is sub-optimal. The controller $K_1(s)$ was implemented

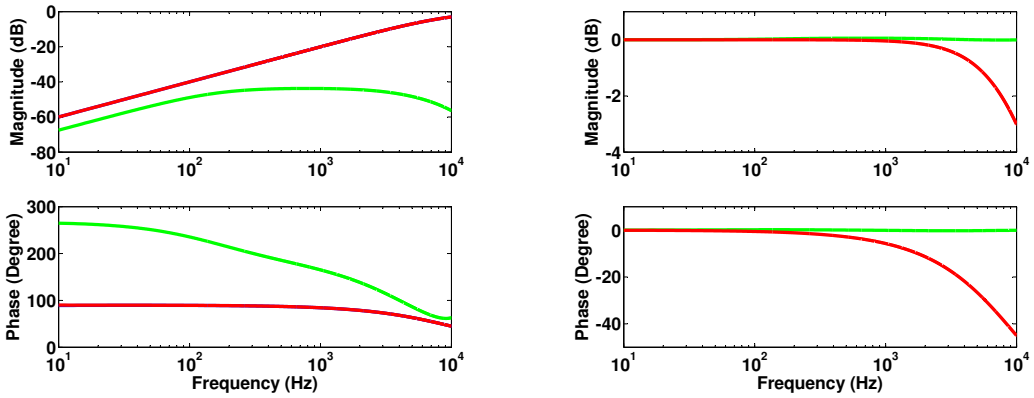

(a) (b)

Figure 6.6: (a) The figure shows the bode plot of the analytical transfer function between F_e and e_F, given by $(1 + K_2(s)G(s)S(s))$, using the robust control framework (green curve) and system inversion process (red curve). The inverse of the weighting function, $W_F(s)$, is shown in blue, which completely overlaps with the red curve (b) The figure shows the bode plot of the analytical transfer function between F_e and $\hat{F}_e$, given by $-K_2(s)G(s)S(s)$, using the robust control framework (green curve) and system inversion process (red curve).

in real-time on National Instruments real time FPGA module. For the estimation of the external input force, F_e, the high order filter $K_2(s)$ was implemented offline.

The analytical transfer function between the external force input, F_e, and the regulation error, e, given by $G(s)S(s)$ comparing the results obtained using the robust control method developed in this paper and the method of system inversion, is shown in Figure 6.5(a). The inverse of the corresponding weight transfer function, $W_s(s)$, which captures the performance objective of constant position regulation is also plotted in Figure 6.5(a). The magnitude part of the Bode plot shows that the transfer function between F_e and e lies below the magnitude of $1/W_s(s)$, thereby achieving good position regulation (as explained in Section 6.1). It can be further seen from the magnitude plots that better position regulation is achieved using the robust control method than system inversion approach as the magnitude of transfer function obtained using robust control remains below that obtained system inversion approach. In Figure 6.5(b), the Bode plot of the analytical transfer function between external force input, F_e, and the control input, u, obtained using the robust control method and the system inversion method is

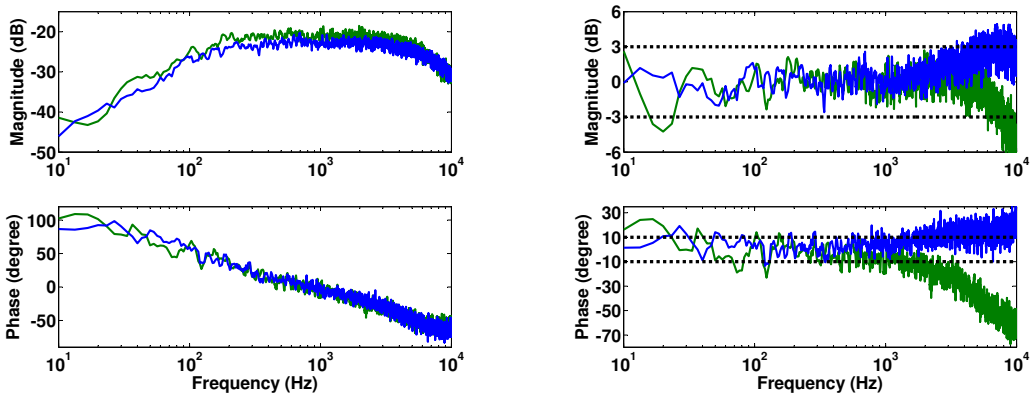

(a) (b)

Figure 6.7: (a) The figure shows the experimentally obtained bode plot of the transfer function between F_e and e, using the robust control framework (blue curve) and system inversion process (green curve). (b) The figure shows the experimentally obtained bode plot of the transfer function between F_e and $\hat{F}_e$, using the robust control framework (blue curve) and system inversion process (green curve).

compared along with the Bode plot of the inverse of the corresponding weighting function, $W_u(s)$, which captures the performance objective of bounded control input. The magnitude part of the Bode plot of transfer function from F_e to u is found to lie below the magnitude plot of $1/W_u(s)$, thereby confirming meeting the performance objective. It is also seen from Figure 6.5(b) that the analytical transfer functions obtained using the robust control and system inversion method almost overlay, thereby indicating that the control effort, u, required in both approaches is almost the same.

As mentioned earlier, the estimation of external force input remains the most important performance objective of constant position optical tweezers. Figure 6.6(a) captures this performance objective by comparing the analytical results obtained using the method of robust control and the system inversion approach. This figure compares the Bode plot of the transfer function from external input force, F_e, to the error in estimation, e_F, obtained using these two methods. It can be clearly seen from the magnitude part of the Bode plot that transfer function obtained using the robust control method lies below the one obtained using the system inversion approach by approximately 10 dB or more at all frequencies upto 10 kHz. This confirms that using controller transfer functions $K_1(s)$ and $K_2(s)$, obtained using the robust control method, can help in using

optical tweezers as a force probe in estimation of external force having high frequency content, over the method of system inversion that itself was shown to be an order in magnitude better (in terms of bandwidth) that the conventional method of force estimation [56]. This claim is further confirmed by looking at the Bode plot of transfer function between external force input, F_e, and its estimate, $\hat{F}_e$, shown in Figure 6.6(b). From this figure, it can be seen that the transfer function between F_e and $\hat{F}_e$ remains very close to unity for the robust control method upto 10 kHz. The magnitude part of the corresponding transfer function for the system inversion case, as seen from 6.6(b), remains within 3 dB value, however as seen from the phase plot, the phase of the transfer function obtained using the system inversion approach, falls rapidly beyond 2 kHz. This indicates the estimate, $\hat{F}_e$, obtained using the system inversion approach is not a good reflection of F_e, if F_e has frequency content above 2 kHz.

The analytical results obtained for the robust control method and the system inversion approach were confirmed by experimental data. The experimentally obtained Bode plots are shown in Figure 6.7(a) and 6.7(b). Figure 6.7(a) shows the experimentally obtained Bode plot of transfer function between F_e and e using the two methods and was found in good agreement with the analytically obtained transfer functions shown in Figure 6.5(a). Figure 6.7(b) compares the experimentally obtained plot between the external force input, F_e, and its estimate, $\hat{F}_e$, obtained using the robust control method and the system inversion method. It was seen in the experiment that the magnitude plot of transfer function remained within 3 dB range upto approximately 6.5 kHz for both the methods. However, from the phase part of Bode plot, it was seen that the phase remained within 10 *degrees* upto 5 kHz for the robust control method and upto 1.5 kHz for the system inversion scheme. Thus, experimentally it was observed that the robust control method helped improve bandwidth of estimation of external force input by over three times of magnitude.

Chapter 7

Conclusion and Discussion

This chapter discusses the overall impact of the research work presented in previous chapters and provides a summary of the contributions made. In this work an alternate paradigm to understand optical tweezers by taking a system theoretic approach is presented. The behavior of optical tweezers system in open loop and in a feedback configuration setting is investigated using controls systems perspective. The main thrust of this research work is to improve the capability of optical tweezers system to be used as a probe for forces having fast changing dynamics. The motivation for this research is bio-assays where bio-molecules are intentionally slowed down by maintaining low concentration of energy molecules well below the native states, in order to measure their dynamics.

As stated earlier in Chapter 1, this work is not an attempt to investigate the performance of optical tweezers system from the fundamental physics viewpoint. However, for understanding purposes, the physics behind optical tweezers is presented in Chapter 2, where a derivation is presented when the microsphere to be trapped is in the Mie regime. The experimental setup used for this thesis is explained in Chapter 3, followed by modeling and characterization of optical tweezers system from a control systems perspective in Chapter 4. The challenges involved in instrumentation of future generation of optical tweezers for high bandwidth force estimation are addressed in Chapter 5 and Chapter 6, where two approaches based on control systems are presented that lead to significant improvement in the bandwidth of external force estimation for feedback enhanced optical tweezers.

Some of the highlights of this work are:

- Construction of an optical tweezers setup with photodiode based sensing, AOD based actuation and FPGA based data acquisition and controller implementation.
  - A single beam optical tweezers system is constructed that uses orthogonal polarization of a plane polarized laser for trapping and detection, thereby avoiding the need to use wavelength specific optics for different wavelengths.
  - The optical tweezers system has a resolution of 2 nm at 30 Hz.
  - The force resolution of the setup is 0.1 pN at 30 Hz.
  - Using the piezo stage, there is a nanometer resolution control on position.
  - This setup supports fluorescence microscopy.
  - Using FPGA for controller implementation, it is possible to implement high order digital controllers.
- Previously unexplained anomaly in the thermal noise power spectrum in constant position optical tweezers for high dc gains is explained in terms of system latencies.
- The input output method of system characterization is introduced to optical tweezers, which enables characterization of individual components of feedback enhanced optical tweezers. Using this method of characterization, the predicted optical tweezers behavior is found to be in very good agreement with the experimental results even at high frequencies.
- Fundamental limitations that limit the scope of using linear feedback schemes in estimating high bandwidth force are analytically explained using system theoretic concepts.
- The challenges involved in estimation of external force input, having high frequency content, using the traditional schemes is discussed.
- The bandwidth limitation of using optical tweezers as a force probe is considerably alleviated by developing a system inversion based methodology which depends on accurately characterizing the optical tweezers system at higher frequencies. Using experimental results it is shown that this method leads to more than an order of magnitude increase in the bandwidth of external force estimation.

- The performance objectives of a constant position optical tweezers are identified, which forms the basis for an optimal scheme to estimate external input force.

- Using robust control, the problem of improving the bandwidth of external force estimation is casted in an H-infinity framework. The results obtained further improve the bandwidth of external force estimation over the system inversion scheme by over three times.

7.1 Future course

The methodologies developed in this work are explained using a language that is intended for both engineers and bio-physicists. This research lays down a foundation to use optical tweezers for investigating bio-molecules having fast time constants, without having the need to considerably slow down the dynamics by artificial means. The next logical step would be to apply the method of system inversion and robust control based estimation for studying the force dynamics of stall forces in DNA processes or investigating the pico-Newton scale forces at play during walk of motor molecules.

The input output method of characterization presented in this thesis for accurately identifying optical tweezers behavior in a feedback setting can be used in constant force optical tweezers to get a better intuition in the locomotion of motor proteins. The problem of estimating the displacement in a force clamp optical tweezer can be casted in the robust control framework to synthesize an optimal strategy of constant force feedback and estimation of fast motor movement.

It is my belief that systems engineering perspective presented here will encourage more people from controls and signal processing community to contribute to micro-manipulation tools that are largely confined to bio-physicists and bio-chemists.

References

[1] G. Binnig, H. Rohrer, C. Gerber, and E. Weibel. Surface studies by scanning tunneling microscopy. *Physics Review Letters*, 49:57–61, 1982.

[2] G. Binnig, C. Gerber, E. Stoll, T. Albrecht, and C. Quate. Atomic resolution with atomic force microscope. *Europhysics Letters*, 3:1281–1286, 1987.

[3] A. Ashkin, J. M. Dziedzic, J. E. Bjorkholm, and Steven Chu. Observation of a single-beam gradient force optical trap for dielectric particles. *Opt. Lett.*, 11:288–290, 1986.

[4] T. Funatsu, T. Harada, M. Tokunaga, K. Saito, and T. Yanagida. Imaging of single fluorescent molecules and individual atp turnovers by single myosin molecules in aquesous solution. *Nature*, 374:555–559, 1995.

[5] Steven M. Block, Lawrence S. B. Goldstein, and Bruce J. Schnapp. Bead movement by single kinesin molecules studied with optical tweezers. *Nature*, 348:348–352, 1990.

[6] Mark J. Schnitzer and Steven M. Block. Kinesin hydrolyses one atp per 8-nm step. *Nature*, 388:386–390, 1997.

[7] M. D. Wang, H. Yin, R. Landick, J. Gelles, and S. M. Block. Stretching dna with optical tweezers. *Biophys. Journal*, 72:1335–1346, 1997.

[8] A. Ashkin. Acceleration and trapping of particles by radiation pressure. *Phys. Review Letters*, 24:156–159, 1970.

[9] Steven Chu, J. E. Bjorkholm, A. Ashkin, and A. Cable. Experimental observation of optically trapped atoms. *Phys. Review Letters*, 57:314–317, 1986.

[10] A. Ashkin and J. M. Dziedzic. Optical trapping and manipulation of viruses and bacteria. *Science*, 235:1517–1520, 1987.

[11] R. M. Simmons, J. T. Finer, H. M. Warrick, B. Kralik, S. Chu, and J. A. Spudich. Use of optical tweezers to measure actin filament movement on hmm (heavy meromyosin). *Advanced experimental medical biology*, 332:331–336, 1993.

[12] Jeffrey T. Finer, Robert M. Simmons, and James A. Spudich. Single myosin molecule mechanics: piconewton forces and nanometre steps. *Nature*, 368:113–119, 1994.

[13] K. Saito, T. Aoki, and T. Yanagida. Movement of single myosin filaments and myosin step size on an actin filament suspended in solution by a laser trap. *Biophysics Journal*, 66:769–777, 1994.

[14] J. E. Molloy, J. E. Burns, J. Kendrick-Jones, R.T. Tregear, and D.C.S. White. Movement and force produced by a single myosin head. *Nature*, 378:209–212, 1995.

[15] A. D. Mehta, R. S. Rock, M. Rief, J. A. Spudich, M. S. Mooseker, and R. E. Cheney. Myosin-v is a processive actin-based motor. *Nature*, 400:590–593, 1999.

[16] C. Veigel, L. M. Coluccio, J. D. Jontes, J. C. Sparrow, R. A. Milligan, and J. E. Molloy. The motor protein myosin-i produces its working stroke in two steps. *Nature*, 398:530–533, 1999.

[17] K. Svoboda, C.F. Schmidt, B.J. Schnapp, and S. M. Block. Direct observation of kinesin stepping by optical trapping interfeometry. *Nature*, 365:721–727, 1993.

[18] K. Svoboda and S. M. Block. Force and velocity measured for single kinesin molecules. *Cell*, 77:773–784, 1994.

[19] S. M. Block. Nanometers and piconewtons: The macromolecular mechanics of kinesin. *Trends Cell Biology*, 5:169–175, 1995.

[20] Koen Visscher, Mark J. Schnitzer, and Steven M. Block. Single kinesin molecules studied with a molecular force clamp. *Nature*, 400:184–189, 1999.

[21] C. L. Asbury, A. N. Fehr, and S. M. Block. Kinesin moves by an asymmetric hand-over-hand mechanism. *Science*, 302:2130–2134, 2003.

[22] C. M. Coppin, D. W. Pierce, L. Hsu, and R. D. Vale. The load dependence of kinesins mechanical cycle. *Proceedings of the National Academy of Science*, 94:8539–8544, 1997.

[23] H. Higuchi, E. Muto, Y. Inoue, and T. Yanagida. Kinetics of force generation by single kinesin molecules activated by laser photolysis of caged atp. *Proceedings of the National Academy of Science*, 94:4395–4400, 1997.

[24] M. J. Schnitzer, K. Visscher, and S. M. Block. Force production by single kinesin motors. *Nature Cell Biology*, 2:718–723, 2000.

[25] S. A. Endow and H. Higuchi. A mutant of the motor protein kinesin that moves in both directions on microtubules. *Nature*, 406:913–916, 2000.

[26] M. Kurachi, M. Hoshi, and H. Tashiro. Buckling of a single microtubule by optical trapping forces: Direct measurement of microtubule rigidity. *Cell Motility and the Cytoskeleton*, 30:221–228, 1995.

[27] R. Yasuda, H. Miyata, and K. Jr. Kinosita. Direct measurement of the torsional rigidity of single actin filaments. *Journal of Molecular Biology*, 263:227–236, 1996.

[28] C. Shingyoji, H. Higuchi, M. Yoshimura, E. Katayama, and T. Yanagida. Dynein arms are oscillating force generators. *Nature*, 393:711–714, 1998.

[29] M. J. deCastro, R. M. Fondecave, L. A. Clarke, C. F. Schmidt, and R. J. Stewart. Working strokes by single molecules of the kinesin related microtubule motor ncd. *Nature of Cell Biology*, 2:724–729, 2000.

[30] T. T. Perkins, S. R. Quake, D. E. Smith, and S. Chu. Relaxation of a single dna molecule observed by optical microscopy. *Science*, 264:822–826, 1994.

[31] T. T. Perkins, D. E. Smith, R. G. Larson, and S. Chu. Stretching of a single tethered polymer in a uniform flow. *Science*, 268:83–87, 1995.

[32] Steven B. Smith, Yujia Cui, and Carlos Bustamante. Overstretching b-dna: The elastic response of individual double-stranded and single-stranded dna molecules. *Science*, 271:795–799, 1996.

[33] c. Bustamante, S. B. S. B. Smith, J. Liphardt, and D. Smith. Single-molecule studies of dna mechanics. *Current opinion in structural biology*, 10:279–285, 2000.

[34] M. W. Berns, W. H. Wright, B. J. Tromberg, G. A. Profeta, J. J. Andrews, and R. J. Walter. Use of a laser-induced optical force trap to study chromosome movement on the mitotic spindle. *Proceedings of the National Academy of Science*, 86:4539–4543, 1989.

[35] W. H. Wright, G. J. Sonek, Y. Tadir, and M. W. Berns. Laser trapping in cell biology. *IEEE Journal of Quantum Electronics*, 26:2148–2157, 1990.

[36] S. Bayoudh, M. Mehta, H. Rubinsztein-Dunlop, N. R. Heckenberg, and C. Critchley. Micromanipulation of chloroplasts using optical tweezers. *Journal of Microscopy*, 203:214–222, 2001.

[37] A. Constable, J. Kim, J. Mervis, F. Zarinetchi, and M. Prentiss. Demonstration of a fiber-optical light-force trap. *Optics Letters*, 18:1867–1869, 1993.

[38] J. Guck, R. Ananthakrishnan, T. J. Moon3, C. C. Cunningham, and J. Kas. Optical deformability of soft biological dielectrics. *Physics Review Letters*, 84:54515454, 2000.

[39] S. Kawata and T. Sugiura. Movement of micrometer-sized particles in the evanescent field of a laser beam. *Optics Letters*, 17:772–774, 1992.

[40] K. Visscher, S.P. Gross, and S.M. Block. Construction of multiple-beam optical traps with nanometer-resolution position sensing. *IEEE Journal of Selected Topics in Quantum Electronics*, 2:1066–1076, 1996.

[41] E. R. Dufresne, G. C. spalding, M. T. Dearing, S. A. Sheets, and D. G. Grier. Computer-generated holographic optical tweezer arrays. *Review of Scientific Instruments*, 72:1810–1816, 2001.

[42] Hullas Sehgal, Tanuj Aggarwal, and Murti Salapaka. Characterization of dual beam optical tweezers system using a novel detection approach. *Proceedings of the American Control Conference*, pages 4234–4239, 2007.

[43] J. C. Crocker and D. G. Grier. Methods of digital video microscopy for colloidal studies. *Journal of Colloid and Interface Science*, 179:298–310, 1996.

[44] S. Kamimura. Direct measurements of nanometric displacements under an optical microscope. *Applied Optics*, 26:3425–3427, 1987.

[45] A. Ashkin and J. M. Dziedzic. Feedback stabilization of optically levitated particles. *Applied Physics Letters*, 30:202–204, 1977.

[46] C. Coppin, J. Finer, J. Spudich, and R. Vale. Detection of sub-8-nm movements of kinesin by high-resolution optical-trap microscopy. *Proceedings of the National Academy of Science*, 93:1913–1917, 1996.

[47] J. E. Molloy, J. E. Burns, J. C. Sparrow, R. T. Tregear, J. Kendrick-Jones, and D. C. White. Single-molecule mechanics of heavy meromyosin and s1 interacting with rabbit or drosophila actins using optical tweezers. *Biophys. Journal*, 68:298S–305S, 1995.

[48] W. J. Greenleaf, M. T. Woodside, and S. M. Block. High resolution, single molecule measurements of biomolecular motion. *Annual Review of Biophysics and Biomolecular Structure*, 36:171–190, 2007.

[49] M. Manosas, J. D. Wen, P. T. X. Li, S. B. Smith, C. Bustamante, I. Tinoco, and F. Ritort. Force unfolding kinetics of rna using optical tweezers. ii. modeling experiments. *Biophysics Journal*, 92:3010 – 3021, 2007.

[50] J. R. Moffitt, Y. R. Chemla, S. B. Smith, and C. Bustamante. Recent advances in optical tweezers. *Annual Review of Biochemistry*, 77:205–228, 2008.

[51] A. Ranaweera and B. Bamieh. Modelling, identification, and control of a spherical particle trapped in an optical tweezer. *International Journal of Robust and Nonlinear Control*, 15:747–768, 2005.

[52] Kurt D. Wulff, Daniel G. Cole, and Robert L. Clark. Servo control of an optical trap. *Optical Society of America*, 46:4923–4931, 2007.

[53] R. M. Simmons, J. T. Finer, S. Chu, and J. A. Spudich. Quantitative measurements of force and displacement using an optical trap. *Biophys. Journal*, 70:1813–1822, 1996.

[54] A. Ashkin. Forces of a single-beam gradient laser trap on a dielectric sphere in the ray optics regime. *Biophys. Journal*, 61:569–582, 1992.

[55] Hullas Sehgal, Tanuj Aggarwal, and Murti Salapaka. Systems approach to identification of feedback enhanced optical tweezers. *Proceedings of SPIE*, 7038:703821–703830, 2008.

[56] Hullas Sehgal, Tanuj Aggarwal, and Murti Salapaka. High bandwidth force estimation for optical tweezers. *Applied Physics Letters*, 94:1531141–1531143, 2009.